

# Coupled Field Problems

Edited by

A. Kassab

*University of Central Florida, USA*

M.H. Aliabadi

*Queen Mary, University of London, UK*

WITPRESS Southampton, Boston



# Contents

Preface	ix
Chapter 1	
Using BEM in glass modelling	
R.M.M. Mattheij, H.G. ter Morsche and K. Wang .....	1
Chapter 2	
Interaction of radiation with other heat transfer modes	
R.A. Bialecki, E. Grela and G. Wöcel .....	39
Chapter 3	
Coupled FVM/BEM approach to conjugate heat transfer	
A. Kassab, H. Li and Y. Ren .....	79
Chapter 4	
Boundary element method, sensitivity analysis and conjugate problems	
C.L. Chan .....	105
Chapter 5	
Aero-thermo-elastic concurrent design optimization of internally cooled turbine blades	
T.J. Martin and G.S. Dulikravich .....	137
Chapter 6	
Dual boundary element formulations for steady state and transient thermoelastic fracture mechanics	
M.H. Aliabadi .....	185
Chapter 7	
Poroelasticity using the BEM	
M. Chopra .....	211

image to  
or

transmitted  
without the

## Chapter 5

### Aero-thermo-elastic concurrent design optimization of internally cooled turbine blades

T. J. Martin & G. S. Dulikravich

*Multidisciplinary Analysis, Inverse Design, and Optimization Lab.  
Department of Mechanical and Aerospace Engineering, Box 19018  
University of Texas, Arlington, USA.*

#### Abstract

This text presents the theoretical methodology, organizational strategy and application of a fully automated computer program for the multi-disciplinary design, optimization and virtual prototyping of internally cooled axial gas turbine airfoils. A three-dimensional cooled turbine airfoil generation program was written to provide automatic transfer of geometric and boundary condition information from the engine cycle, aero-thermal, heat conduction, thermo-fluid and thermo-elastic analysis programs. The set of optimization design variables defined the geometry, internal coolant passage configuration, internal heat transfer enhancements, coolant supply pressures and turbine inlet temperature. A constrained optimization algorithm was used to control the thermal optimization process to maximize the cooling effectiveness or engine specific thrust subject to material integrity and durability constraints. The constrained optimization problems required 300-800 objective and constraint function analyses. The boundary element method (BEM) was used to solve the non-linear heat conduction equation iteratively coupled to a computational fluid dynamics (CFD) code for the conjugate prediction of the heat transfer between the hot gas and the solid blade. A compressible system of fluid elements was developed for the serpentine coolant network to calculate the pressure losses, flow rate and heat balance between the blade and coolant fluid. The BEM temperature field was analyzed to maintain material integrity and to maximize blade durability against creep and corrosion. A two-dimensional thermo-elastic BEM code was developed for the enforcement of the thermo-mechanical fatigue (TMF) constraint. Implicit differentiation of the thermal and thermo-elastic solvers was performed to compute design sensitivity derivatives faster and more accurately than via explicit finite differencing. A factor of three savings of computer processing time was realized for two-dimensional problems and a factor of twenty was obtained for three-dimensional problems, but the program's memory requirements were doubled. Results have shown that a significant increase in engine performance can be achieved with computer automation of the turbine cooling design optimization process.

## 1 Introduction

The greatest efficiency improvements in gas turbine engines are likely to be accomplished by increasing the rotor speed and turbine inlet temperature. Higher rotor speeds can contribute directly to higher thrust-to-weight ratios and more compact engines by allowing more power to be extracted from each turbine stage. Unfortunately, the maximum centrifugal loads in the rotor blade generally set the angular speed limit for a given tip radius of a blade that is to be manufactured from a given type of material. Although it is desirable to maximize the turbine blade's durability by minimizing cycle fatigue, this type of thermo-structural optimization is beyond the scope of this research for other reasons. First, the quantification of the engine performance with respect to the rotor speed is intrinsically related to a rigorous modeling of the compressor. Second, highly non-linear aero-elastic modeling, being necessary to predict fatigue life limited by vibratory stresses, is prohibitively expensive for computational automation. On the other hand, the practical benefits of computer automated maximization of the temperature while maintaining material integrity can be done with fewer resources and with more reliable and existing software codes.

The advantages of increasing the turbine inlet temperature can be demonstrated by examining its effect on a standard engine performance parameter, such as specific thrust. Due to the increased amount of energy released by combustion, the specific thrust increases continuously with an increase in the turbine inlet temperature for all engine classifications, assuming that all other variables such as flight Mach number and air mass flow rate are held constant (Lakshminarayana [1]). The thrust-specific fuel consumption is another performance parameter which is important for civil transport aircraft engines, that is, fuel economy. The proportionality of temperature to specific fuel consumption is a little more complicated because higher temperature drops allow larger amounts of power to be extracted by the turbine. Given that each compressor stage is designed at its operational limit as defined by the maximum stall pressure ratio, the optimum compressor pressure ratio is dependent upon that available power. Ultimately, increasing the turbine inlet temperature has a favorable effect on fuel economy. In addition, greater temperature drops per stage can lead directly to more compact engines. Thus, increasing the turbine inlet temperature optimizes all engine performance parameters such as specific thrust, thrust-specific fuel consumption and engine weight. Typically, a 1% increase in turbine inlet temperature can produce a 3% to 4% increase in engine output (Hill & Peterson [2]; Brown et al. [3]).

There is an obvious thermal limit in the turbine because of melting, oxidation and sulfidation (hot corrosion) of the blades, not to mention that the increased temperature environment in the presence of high centrifugal and bending loads increases the stresses, adversely affects the blade life due to thermally-enhanced creep, thermo-mechanical fatigue caused by cyclic stress and high temperature gradients that induce cracking, thermal barrier coating delamination and plastic thermal strains. Thus, the temperature in the turbine has a more broad effect on engine performance. For these reasons, this research has focused only upon the computer-automated aerodynamic and thermal optimization of the turbine with the application of thermal integrity, oxidation life, structural integrity and thermo-mechanical fatigue life constraints at a fixed rotor speed.

## 1.1 N

A  
 $D_h$   
 $e_s$   
 $\epsilon$   
 $f$   
 $F$   
 $G$   
 $G_{cool}$   
 $\gamma$   
 $H$   
 $h_{cool}$   
 $h_o$   
 $\eta$   
 $k$   
 $\dot{m}$   
 $\dot{m}_f$   
 $M$   
 $\mu$   
 $\rho$   
 $s$   
 $p_o$   
 $P_{t,cool}$   
 $\pi_c$   
 $Q$   
 $r$   
 $R_K$   
 $\sigma_{ij}$   
 $t_s$   
 $T$   
 $\bar{T}$   
 $T_{t,cool}$   
 $T_{t,inlet}$   
 $T_{max}$   
 $T_o$   
 $T_O$   
 $V_i$   
 $w$   
 $W$   
 $\Omega$   
 $x_s$

## 1.1 Nomenclature

$A$	Cross-sectional area of a coolant passage
$D_h$	Hydraulic diameter of a coolant passage
$e_s$	Strut fillet radius
$\varepsilon$	Coolant passage wall roughness or trip strip height
$f$	Friction factor
$F$	Optimization objective function
$G$	Inequality constraint function on the optimization
$G_{\text{cool}}$	Mass flow rate of coolant fluid
$\gamma$	Ratio of specific heats of an ideal gas
$H$	Equality constraint function on the optimization
$h_{\text{cool}}$	Heat transfer coefficient on coolant passage walls
$h_o$	Heat transfer coefficient on outer turbine airfoil surface
$\eta$	Cooling effectiveness or convection efficiency
$k$	Thermal conductivity coefficient
$\dot{m}$	Air mass flow rate through engine
$\dot{m}_f$	Mass flow rate of fuel
$M$	Mach number
$\mu$	Coolant fluid viscosity coefficient
$\rho$	Density of coolant fluid
$s$	Turbine airfoil contour following coordinate
$p_0$	Stagnation pressure
$p_{t,\text{cool}}$	Coolant fluid inlet total pressure
$\pi_c$	Stagnation pressure ratio across compressor
$Q$	Heat flux
$r$	Streamwise (radial) direction of coolant flow
$R_K$	Coolant pressure loss coefficient in a $180^\circ$ turning bend
$\sigma_{ij}$	Stress tensor
$t_s$	Strut thickness
$T$	Temperature
$\bar{T}$	Average or target temperature
$T_{t,\text{cool}}$	Bulk total temperature of coolant
$T_{t,\text{inlet}}$	Turbine inlet total temperature
$T_{\text{max}}$	Maximum temperature in turbine blade metal
$T_0$	Stagnation temperature
$T_O$	Temperature on outer turbine airfoil surface
$V_i$	Vector of optimization design variables
$w$	Coolant fluid average local speed
$W$	Coolant passage wall thickness
$\Omega$	Engine rotation rate
$x_s$	Coordinate of strut centerline intersection with turbine airfoil

## 1.2 Turbine cooling techniques

With presently available materials such as nickel-based alloys, turbine blades cannot withstand metal temperatures in excess of 1300 K. Turbine inlet temperatures of modern engines already exceed this amount, especially for high-speed aircraft, because internal and external cooling of the turbine blades allows those higher gas temperatures. Modern turbomachinery rotor and stator blades have traditionally been cooled by directing compressor bleed air through passages in the engine and into complex serpentine-like coolant flow passages inside the blades (Mochizuki et al. [4]). Much of the cooling is accomplished via convection on the coolant passage surfaces. Typically, the cooling air provides a heat sink that is only 400 to 450 K cooler than the maximum metal temperature. The incorporation of internal cooling and improvements in materials have resulted in increases in turbine inlet gas temperatures from 850 K in the 1960s to 1600 K today, with about 350 K of this increase attributed to the cooling devices alone (Kawaike et al. [5]; Ikeguchi & Kawaike [6]). Internal cooling of turbine blades has been a major focus in modern turbomachinery and manufacturing for over thirty years. For classical blade materials and geometric design it has been effective for turbine inlet gas temperatures up to approximately 1560 K. The more recent external (film) cooling techniques allow even greater inlet gas temperatures of up to 1800 K. Film cooling can produce a protective layer of cool air on the surface of the blades, but more cooling air bled from higher compressor stages are necessary, and they result in greater external pressure losses due to a reduction in the boundary layer momentum. Moreover, with the current efforts to push the inlet turbine gas temperatures even higher, an opposite effect becomes significant. This is the production of NO<sub>x</sub> that starts occurring at high temperatures. Consequently, there is renewed interest in exploring the possibilities of better closed-loop high-pressure internal cooling schemes. Because of the computational complexities involved, film cooling was not incorporated into this research, and focus has been exclusively upon internal cooling techniques.

All of the internal cooling techniques involve increased aerodynamic losses and decreased efficiency resulting from the bleeding of air from the compressor. External losses are associated with a loss of power from the coolant flow and increased profile losses due to thicker blades arising from the coolant holes. Generally, the greater the coolant flow rate, the more the blades are cooled, but the result is an even greater pressure loss in the coolant passages. Heat transfer enhancements, such as trip strips or turbulators, impingement cooling, tube banks and miniature heat exchangers, can provide further enhancements to the amount of internal convection heat transfer, but they invariably result in disproportionately more pressure loss. In addition, the pressure losses due to the mixing of the coolant with the external flow results in a steady decrease in the net turbine efficiency as the turbine inlet temperature increases (Brown et al. [3]). After considering the effect on aerodynamic efficiency of film cooling and coolant air ejection, it may even worsen the performance of the engine. Also, when bleeding coolant air from the compressor, if the fuel flow rate to the burner is not reduced accordingly, the turbine inlet temperature will be magnified by the same mechanism that allows the blades to handle those higher temperatures. Thus, the advantages of increasing the turbine inlet temperature by internal cooling are offset by the aerodynamic losses, as well as the mechanical and manufacturing complexities of the internal cooling passages. Despite all these difficulties, a considerable gain in turbine performance may be realized to offset all those penalties. So the question is, how can engineers design and optimize an internal turbine blade cooling system?

Dur  
develop  
cooling  
passage  
demon  
(Kenno  
Dulikra  
Martin  
three-di  
by spec  
configu  
An opt  
passage  
specific  
shape d  
bounda

This  
the geo  
involve  
cooled  
that the  
perform  
example  
thicknes  
of the b  
blade f  
manual  
is not y  
At the  
remains  
simultar  
maintain  
costs ar  
these q  
simultar  
(MCAD

## 1.2 MC

Figure 1  
the MC/  
informat  
UNIX C  
algorithm  
used sev  
values f  
responsi

During the past fourteen years, Dulikravinich and his research team of graduate students have developed a fully-automatic computational inverse shape design algorithm that allows a cooling systems designer to determine the numbers, sizes, shapes and locations of coolant flow passages within internally cooled configurations. The methodology was successfully demonstrated on multi-holed two-dimensional turbine airfoils with thermal barrier coatings (Kennon & Dulikravinich [7]; Chiang & Dulikravinich [8]; Dulikravinich & Kosovic [9]; Dulikravinich & Martin [10]), single-holed three-dimensional turbine blades (Dulikravinich & Martin [11]), scramjet combustor struts (Dulikravinich [12]), and hydrogen cooled multi-coated three-dimensional rocket nozzle walls (Martin & Dulikravinich [13]). This methodology worked by specifying a desirable variation of heat flux over the external surface of the cooled configuration, in addition to the boundary conditions of a well-posed heat conduction problem. An optimization algorithm was then used to modify iteratively the shapes of the coolant passages in an attempt to minimize the squared sum of the difference between the user-specified and numerically computed heat fluxes on the outer boundary. The inverse thermal shape design process continued until the difference between the computed and over-specified boundary conditions converged to a user-specified tolerance.

This inverse thermal shape design methodology worked, but in view of the complexities of the geometry, the intricately coupled engine components and the numerous parameters involved in a turbine, the efficacy of the method fell short of the real objectives of internally cooled turbine blade design. Designers of high-performance jet engines have long recognized that the final design of a turbine blade must represent a compromise among aerodynamic performance, cooling effectiveness, structural integrity, durability and manufacturability. For example, improvements in aero-thermodynamic performance can be realized by reducing blade thickness, but eventually a hard structural design constraint is reached. Either the fatigue life of the blade becomes unacceptably low because of excessive flow-induced vibrations, or the blade flutters with immediate destructive consequences (Bendiksen [14]). Even with the manual design process currently operating in the turbomachinery industry, a systematic method is not yet available for full understanding of cooled turbine efficiency (Lakshminarayana [1]). At the present time, testing is the only reliable method. Thus, the following question still remains, "Is it possible to design manufacturable turbine cooling configurations that simultaneously increase the turbine inlet temperature, decrease the coolant requirements, maintain material integrity and improve airfoil durability, so that engine capital and operating costs are reduced?" This research presents a methodology that proposes to answer some of these questions, and addresses as many of these goals and constraints as possible simultaneously by using our multidisciplinary computer automated design optimization (MCADO).

## 1.2 MCADO system for internally cooled turbine blades

Figure 1 illustrates how information flows among the main computational components within the MCADO system for internally cooled turbine blades. Boundary condition and parameter information is fed either iteratively or non-iteratively between FORTRAN subroutines using UNIX C-shell scripts, common blocks and argument lists. The constrained optimization algorithm, called OPTRAN, is the main driver program for the MCADO system. OPTRAN used several popular numerical optimization packages to minimize the objective function values for a population of design vectors subject to a finite number of constraint functions. It is responsible for perturbations to the design vector using information received from the

numerical analysis and design programs. This hybrid constrained optimization package was discussed in a recent publication involving genetic and evolutionary optimization algorithms (Dulikravich et al. [15, 16, 17, 18, 19]).

The design variable set defines the geometry of the turbine blade including the external turbine airfoil shape definition, thermal barrier coating thickness, blade wall thickness distribution and blade internal strut configurations. The blade stacking axis, twist and taper are incorporated into the design variable set for three-dimensional blades. Other design variables that do not affect the geometry, such as the turbine inlet temperature, coolant mass flow rate and heat transfer enhancements such as trip strip height, transverse rib spacing and tube bank diameter, are also shown in Figure 1. With a constrained optimization algorithm, the internally cooled turbine blade designs were modified so that the turbine cooling network can handle sequential increases in the turbine inlet temperature with an appropriate amount of coolant air bleed and internal heat transfer enhancement (Martin et al. [20]).

Various aerodynamic and thermal objective functions were attempted with the MCADO system. The objective of the optimization process, shown in the upper-right-hand corner of Figure 1, was quantified as a single scalar function. The aerodynamic objective functions used the CFD-calculated pressure and temperature fields. The thermal objective function used only the calculated temperature field in the turbine blades. In more recent efforts, a fluid element system simulated the internal coolant flow and an engine cycle analysis determined the impact of the design variables on the real engine efficiency so that either the engine specific thrust or thrust-specific fuel consumption was optimized. That engine cycle program requested information about the engine operating conditions, such as flight Mach number, altitude, air intake, rotor speed and component efficiencies (inlet, compressor, burner and nozzle). These conditions were fixed during the optimization process, in addition to the design variables coming from the main optimization algorithm (see upper left corner of Figure 1). The compressor stagnation pressure ratio was not a design variable, but it was a function of the turbine inlet temperature because, as it increased, the turbine extracted more shaft power to drive the compressor. Therefore, a sub-optimization procedure was implemented within the engine cycle analysis using the golden section method (Press et al. [21]) to maximize the specific thrust with respect to the compressor pressure ratio. The turbine efficiency was also considered to be a function that depended upon a numerical aero-thermal analysis of the hot gas flow through the turbine blade row. That conjugate aero-thermal analysis will be described later. It is understood that the engine cycle analysis (objective function) is strongly affected by the turbine inlet temperature, so Figure 1 shows the inlet temperature as the primary design variable. The process of extracting coolant air from the compressor was also incorporated into the cycle analysis code, affecting both the compressor and turbine efficiencies.

When aerodynamic shape optimization was involved, the external turbine airfoil shape was included in the design variable set coming from the constrained optimization program. The development of the aerodynamic objective function required grid generation in the turbine blade row, as well as a CFD prediction of the hot gas flow-field through the blade row. The aerodynamic objective was quantified by the total pressure loss function, shown as turbine efficiency (Petrovic et al. [22]; Dennis et al. [23]), that was subsequently fed back into the engine cycle analysis (Brown et al. [3]). When the MCADO system operated on a stationary blade such as a guide vane or a stator, this CFD calculation could not provide a measure of the turbine efficiency, and so the aerodynamics did not directly affect the objective function. In those cases, the CFD calculation was executed only once on a fixed blade shape and the objective was strictly a thermal one.

F

C  
C

S

The  
that cou  
material  
coupling  
informat  
tempera  
The bou  
a multip  
generati  
coolant  
that can  
the heat  
adjusted  
design v  
entered  
converge  
heat tra  
coolant)



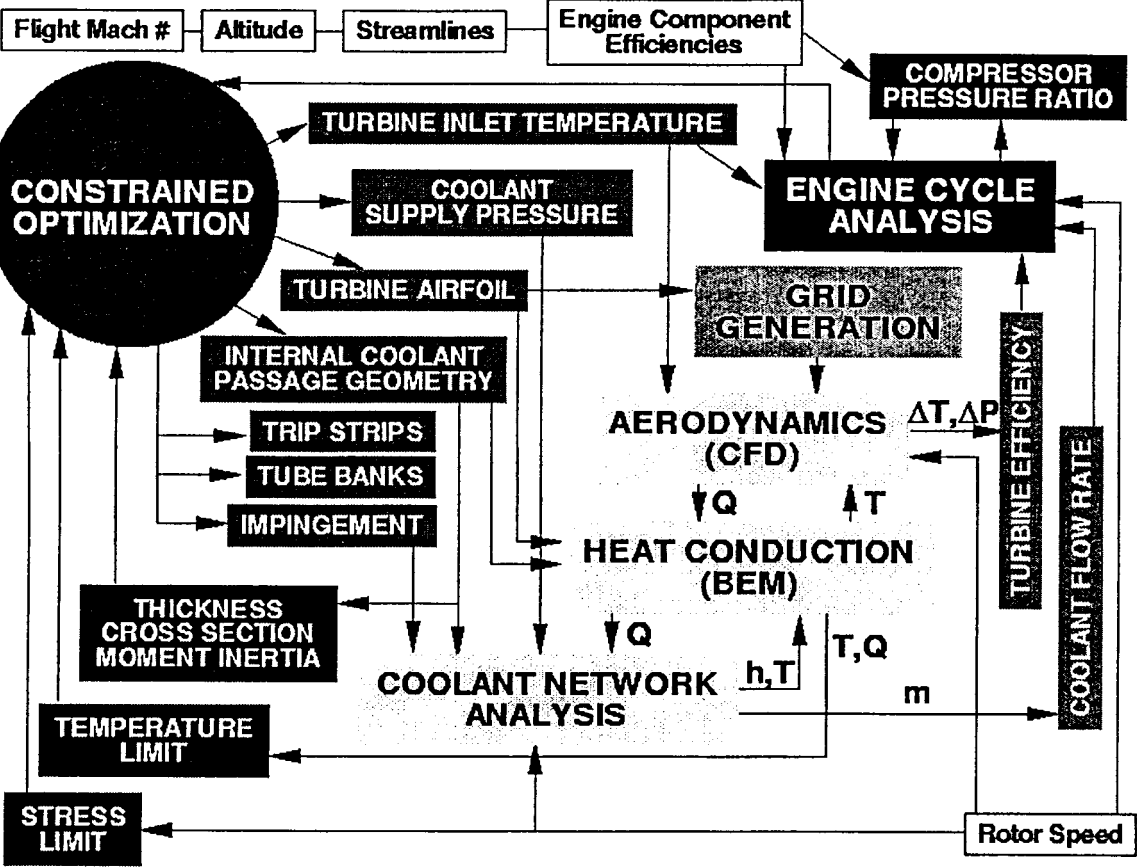


**Figure 1: Flow chart for MCADO of internally cooled turbine blades.**

The temperature field was determined by a conjugate aero-thermo-fluid numerical analysis that coupled the hot gas flow external to the blade, the heat conduction in the solid blade material and the coolant flow in the internal coolant flow passages. Figure 1 shows an iterative coupling of the three computational components by transferring boundary condition information (temperature  $T$ , heat flux  $Q$ , heat transfer coefficients  $h$  and bulk coolant temperatures,  $T_c$ ) between them. Any CFD code could be used for the aerodynamic analysis. The boundary element method (BEM) was used to solve the steady heat conduction equation in a multiply coated blade with temperature-dependent material properties. It did not require grid generation inside the blade material. The boundary condition information on the internal coolant passage surfaces existed as heat transfer coefficients and as bulk coolant temperatures that came from a fluid element analysis of an arbitrary coolant network (COOLNET). Since the heat flux into the blade heated the coolant fluid, the bulk coolant temperatures were adjusted during the iterative process. The coolant flow rate and heat transfer enhancement design variables (trip strips and tube banks) from the main constrained optimization program entered into this sub-program. With each iteration, the CFD was executed to partial convergence while the other two components were factored. The overall iterative conjugate heat transfer prediction process among the three components (hot gas, blade material and coolant) completed when the heat flux residual converged.

During the iterative numerical optimization process, the material and structural integrity of the blades was not compromised. The maximum temperature inside the blade was maintained with the enforcement of equality constraint functions and with optimization search directions controlled via projection methods (Foster & Dulikravich [24]). The maximum temperature was a consequence of the coupled CFD/BEM/COOLNET aero-thermo-fluid analysis. A constrained sub-minimization process restored any active or violated constraint functions until a thermally feasible design was reached. Thermal feasibility was defined as a condition when the maximum temperature on the blade surface was less than the melting or limiting oxidation temperature of the blade material. Obviously the performance demands of gas turbine engines must be within the limitations set by the materials used in its construction. Turbine rotor blades are seldom designed to avoid outright failure, but rather to avoid failure within a specified time. Turbine blades are designed to handle four kinds of stresses; centrifugal, bending, vibratory, and thermal. Since we are dealing with a fixed rotor speed and because approximate stress calculations can be justified, a centrifugal stress constraint was enforced by setting a lower limit to the radial cross-sectional area of the blade. Tilting the blade to induce a centrifugal bending in the opposite direction as the pressure load offset the bending stresses. Therefore, given a fixed load, the bending stress constraint was ignored. The thermal stress environment provided an estimate for the mean creep life of the blade, which was subsequently constrained to some minimum life span. Durability limitations caused by steady-state thermo-mechanical fatigue required a two-dimensional thermo-elastic analysis and they were similarly constrained given a number of cycles until failure.

If blade flutter was to be of major concern to the turbine design group, the aero-elastic solution procedure may require a nonlinear dynamic analysis of the blade's structure under transient aerodynamic loads. Full non-linear and time-accurate computational aerodynamics and elasto-dynamics codes are still prohibitively expensive for MCADO. Even reduced-order models are still too expensive, while linearization cannot predict stall flutter, shock-induced oscillations and bending/torsion coupling. A linear dynamic perturbation of a steady aerodynamic analysis may be adequate to resolve transonic shock-induced flutter (Dowell [25]), but even this method is beyond the scope of this research. At the very least, a modal analysis of the blade is necessary to determine its natural vibrational modes. Therefore, aeroelasticity analysis involving fluid-structure interaction will not be addressed here. Instead, simpler structural constraints were used to ensure that the blade's vibrational modes were avoided. Geometric functions such as wall thickness, cross-sectional area and moment of inertia provided an approximate upper limit to maintain structural integrity.

The temperature field ( $T$  &  $Q$ ) computed by the numerical heat conduction analysis (or by a conjugate analysis) was fed one way into a BEM thermo-elasticity algorithm. The BEM was also used for this thermo-elastic analysis because it did not require internal mesh generation. The result of this computation was the thermo-elastic deformation and the thermal stress fields. It has been proven that these displacements (blade deformations) do not significantly affect the resulting heat conduction in the blade. Therefore, the coupling of the heat conduction and thermo-elastic solvers was not iterative.

Objective and constraint information, as well as design sensitivities of those functions with respect to the design variables, were fed back to the main constrained optimization program. The hybrid evolutionary optimization algorithm then determined one or more perturbations to the design variable population, and each required additional objective and constraint function evaluations for the next cycle. The global optimization process proceeded until user-specified tolerances or goals were met. Acceptance of the final design was ultimately the responsibility

of the  
have be

### 1.3 Par

The pa  
now be  
comple  
struts'  
variabl  
definiti  
stackin  
geomet  
outer su

The  
of the  
determi  
followe  
edge (F  
constan  
(Barsky  
distance  
number

Nex  
coordin  
defined  
one to t  
In addit  
trailing  
modelin  
definitic  
cutback

The  
to devel  
generate  
impinge  
illustrati  
the full t

of the cooling systems design engineer who runs the MCADO system, but the repetitive tasks have been left to the computer.

### 1.3 Parametric model of the turbine airfoil geometry

The parametric model of the internally cooled and thermal barrier coated turbine blade will now be discussed in greater detail. The set of two-dimensional optimization design variables completely defined the shape of the thermal barrier coating, wall thickness variation, internal struts' locations, struts' thicknesses, and their corner fillets. The three-dimensional design variables defined the number of blades in the rotor or stator blade row, the periodic endwall definition for the stream tube, pitch of the leading and trailing edge impingement holes and stacking of sectional airfoil shapes. The turbine airfoils were defined using a conventional geometric definition similar to those used by most industrial turbine design teams. The blade outer surface shape was kept fixed during the internal cooling scheme optimization.

The first step in the development of the multiple coolant flow passages was the description of the cooling wall thickness function. The wall thickness function's ordinate,  $W(s)$ , determined the thickness of the wall between the hot gas and coolant fluid. The abscissa followed counter-clockwise along the metal/coating interface,  $s$ , from trailing edge to trailing edge (Figure 2), where the local coordinate system  $(x,y)$  was fixed upon a curved surface at a constant radius from the engine axis.  $W(s)$  was defined by a piecewise-continuous  $\beta$ -spline (Barsky [26]) curve that varied in the direction normal to the metal/coating interface to a distance controlled by one design variable per  $\beta$ -spline control vertex. For this research, the number of coolant flow passages in the turbine blade was kept fixed.

Next came the specification of the locations of the internal strut centerlines. The  $x$ -coordinates of the intersections of the strut centerlines with the outer turbine airfoil curve were defined as  $x_{Ssi}$  and  $x_{Spi}$  for the suction and pressure sides, respectively. The index  $i$  varied from one to the number of struts,  $N_{strut}$ . The range over which each strut could vary was  $\pm \Delta x_{Si}$ . In addition to the coordinate of the struts, the strut thickness,  $t_{Si}$ , and a fillet radius on either the trailing or leading edge sides,  $e_{Sli}$  and  $e_{Sli}$  respectively, were used to complete the geometric modeling of each strut. The trailing edge slot is shown on the right hand side of figure 2. The definition of the slot included the slot width, slot length, pressure-side wall thickness and cutback distance.

The virtual geometric parameterization of the turbine airfoil described previously was used to develop two-dimensional sectional geometries. Several other parameters were needed to generate the three-dimensional blade. This included tip cap thickness, tip turn radius, and impingement hole radii and pitches at the leading and trailing edge ribs. Figure 3 is an illustration of a typical thermal barrier coated cored axial turbine blade section on the left and the full three-dimensional stacked blade on the right.

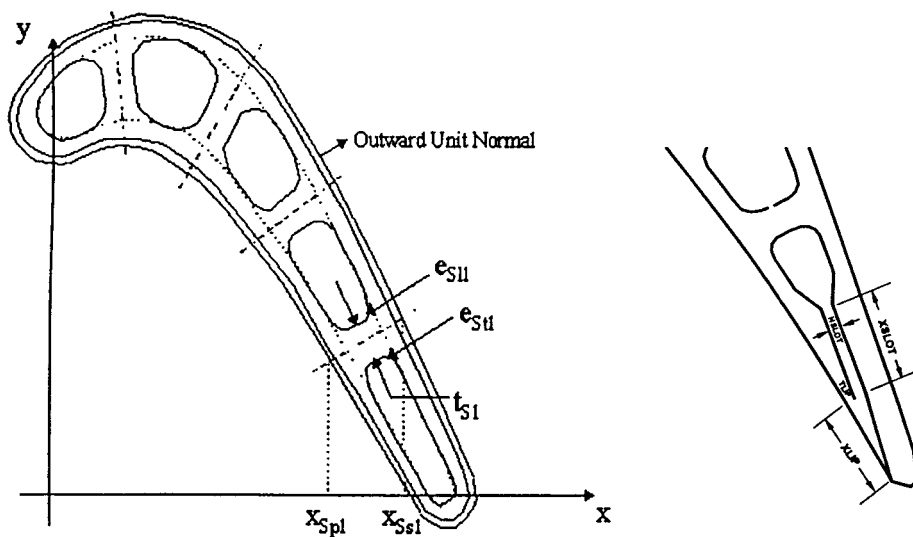


Figure 2: Turbine airfoil, thermal barrier coating and coolant passage geometry. The airfoil contour and coating/metal interface are shown as solid lines. The cooling wall thickness function is used as a reference (dotted line) to draw the coolant passage walls (solid lines).

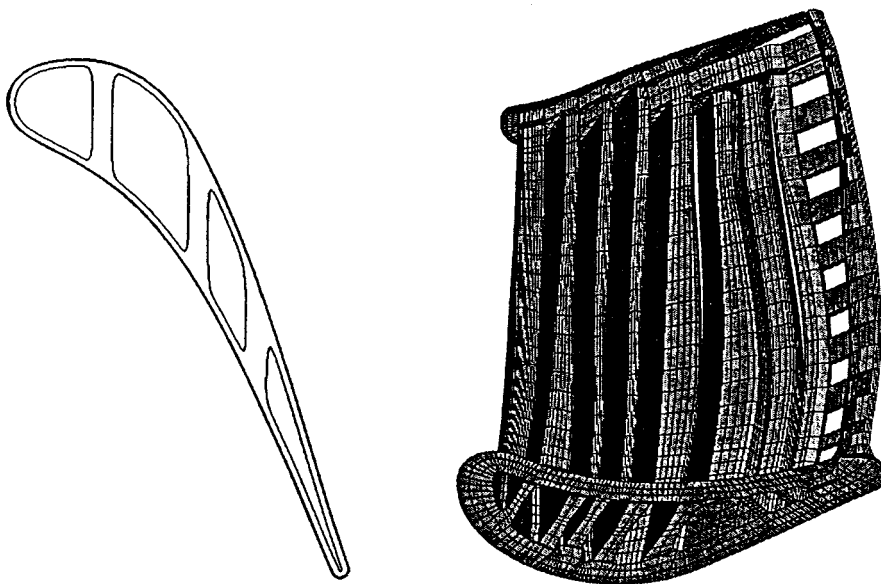


Figure 3: Boundary element discretization of an internally cooled and thermal barrier coated axial gas turbine blade showing the sectional airfoil shapes and a surface mesh.

## 2 Opt

A cons  
FORTH  
algorith  
each ne  
populat  
includi  
and a  
 $H_n(V)$   
saved i

This  
the Dav  
(Goldbe  
simulat  
optimiz  
during  
into the  
minimiz

The  
function  
generati  
guided  
& Dulik  
via the  
minimiz  
feasible

The  
to the v  
evolved  
several  
(1) The  
(2) The  
(3) The  
deco  
con

### 2.1 Obj

The prin  
that asse  
optimiza  
different  
oxidatio  
optimiza

## 2 Optimization of internally cooled turbine airfoils

A constrained evolutionary hybrid optimization computer program has been developed in the FORTRAN programming language (Martin et al. [16, 20]; Dulikravich et al. [19]). This algorithm creates sequential populations of feasible design variable sets,  $\{V\}$ , that evolve with each new optimization cycle by minimizing the objective function,  $F(V)$ , associated with  $N_{\text{pop}}$  population members. These design variables are subject to a finite number of constraints, including lower and upper bounds on the design variables,  $\{V_{\text{min}}\}$  and  $\{V_{\text{max}}\}$ , respectively, and a finite number of inequality and equality constraint functions,  $G_m(V) < 0$  and  $H_n(V) = 0$ . Only feasible sets of design variables from the current optimization cycle are saved into the population matrix,  $[\{V_1\}, \{V_2\}, \dots, \{V_{N_{\text{pop}}}\}]$ .

This new hybrid optimization program incorporates four popular optimization algorithms; the Davidon-Fletcher-Powell (DFP) (Davidon [27]) gradient search, a genetic algorithm (GA) (Goldberg [28]), the modified Nelder-Mead (NM) (Nelder & Mead [29]) simplex method, and simulated annealing (SA) (Press et al. [21]). Each technique provides a unique approach to optimization with varying degrees of convergence, reliability and robustness at different cycles during the iterative optimization procedure. A set of rules and switching criteria were coded into the program to switch back and forth among the different algorithms as the iterative minimization process proceeded (Dulikravich et al. [19]).

The evolutionary hybrid scheme handled the existence of equality and inequality constraint functions in three ways: Rosen's projection method, feasible searching and random design generation. Rosen's projection method (Hafka & Gurdal [30]) provided search directions that guided descent-directions tangent to active constraint boundaries. In the feasible search (Foster & Dulikravich [24]), designs that violated constraints were automatically restored to feasibility via the minimization of the active global constraint functions. If at any time this constraint minimization failed, random designs were generated about the current design until a new feasible design was reached.

The population matrix was updated every iteration with new designs, and ranked according to the value of the objective function. As the optimization process proceeded, the population evolved towards the global minimum. The optimization problem was completed when one of several stopping criteria was met:

- (1) The maximum number of iterations or objective function evaluations were exceeded.
- (2) The best design in the population was equivalent to a target design.
- (3) The optimization program tried all four algorithms but failed to produce a non-negligible decrease in the objective function. The latter criterion was the primary qualification of convergence and it usually indicated that a global minimum had been found.

### 2.1 Objective function formulations

The primary goal of this section is to describe how to establish a quantifiable objective function that assesses the performance and durability of internally cooled configurations for numerical optimization. In order to arrive at the most effective thermal optimization strategy, three different classifications of thermal objective functions have been developed: (1) oxidation/corrosion minimization, (2) coolant effectiveness maximization and (3) engine cycle optimization.

### 2.1.1 Oxidation/corrosion objective

The oxidation/corrosion minimization strategy made use of an objective that closely resembled one from inverse thermal shape design. At the high temperatures experienced in a turbine, corrosion and oxidation damage affects the life of the airfoil. The addition of thermal barrier coatings and age hardening materials such as chromium and cobalt to the nickel-based turbine blade alloys makes the part resistant to material corrosion. But these materials are expensive, and at the high temperatures experienced by the turbine blades, corrosion still affects the blade life by thinning its walls and weakening the material. Sulfidation is a corrosion phenomenon that results from the condensation of sodium sulfate on the surface of the blade. With increasing surface temperature, the corrosion rate first increases and then decreases because the temperatures are nearer to the vapor pressure of the sodium sulfate and less condensation occurs. In regions where surface temperatures are extremely high, surface atoms react with oxygen and oxidation occurs, and oxidation increases with increasing temperature. Therefore, turbine airfoil life expectancy is at a maximum at a specific temperature,  $\bar{T}$ . Therefore, the integrated difference between the computed temperature and user-specified target or mean temperature,  $\bar{T}$ , was minimized. The numerical optimization algorithm was used to modify the coolant passage configuration in order to minimize the squared difference between the local computed temperature and the target temperature. The integration was either carried out over the solid domain,  $\Omega$ .

$$F(V_i) = \int_{\Omega} (T - \bar{T})^2 d\Omega \quad (1)$$

As this function was minimized, the temperature field within the turbine blade approached the desired value and producing a more uniform temperature distribution. The primary outcome of this is the maximization of the oxidation/corrosion life, but it also resulted in a reduction in the thermal stresses. The domain-integrated temperature also had the added advantage of minimizing weight. Unfortunately, it required the resolution of the internal temperature field, a post-processing procedure with the boundary element method, and it requires an internal mesh. Minimization of the boundary-integrated function yielded more uniform temperature fields without the additional difficulties, but the optimization process did not necessarily result in a reduction in weight.

The behavior of this objective was very sensitive to the user-specified target temperature,  $T$ . High target temperatures tended to result in lower heat fluxes absorbed by the blade, but they resulted in thicker coolant walls with increased coolant requirements. This tendency was true because the internal surfaces generally have higher heat transfer coefficients and greater surface area exposed to a fluid. Low target temperatures produced less uniform temperature fields because of the maximum temperature equality constraint, thinned the coolant walls and increased the heat flux.

### 2.1.2 Maximization of the cooling effectiveness

Although the uniform temperature objective did have some desirable features that will be demonstrated later, it has been concluded that it does not consistently satisfy the criterion established for internal turbine coolant passage optimization. With a thermal objective function alone, one can focus only upon one goal. Therefore, we must choose whether we wish to reduce the cooling requirements, improve the airfoil's durability or increase the turbine inlet temperature. The maximization of the cooling effectiveness was tried as one more alternative.

Here  $T_c$   
metal te

In al  
blade.  
tempera  
The opt  
because  
the resu  
leading  
increas  
perform  
function  
closed-c

2.1.3 Op  
An engin  
in order  
cooling  
importan  
thrust (e  
specific

$F(V) =$

Here, in  
the turbin  
inlet,  $Q_R$   
The optim  
found by

$$\eta = \frac{T_{\text{cout}} - T_{\text{cin}}}{T_m - T_{\text{cin}}} \quad (2)$$

Here  $T_{\text{cin}}$  is the bulk coolant temperature at the inlet to the coolant passages,  $T_m$  is the blade metal temperature and  $T_g$  is the hot gas temperature.

In all cases studied, the maximum cooling effectiveness increased the heat flux into the blade. The internal heat transfer coefficients were increased to their upper limit, the bulk temperatures of the coolant became higher and the coolant walls became as thin as possible. The optimized design dramatically increased the pressure losses in the coolant passages, because the objective favored high heat transfer coefficients. This increased heat transfer was the result of increased wall roughness and there were large increases in the heat flux at the leading and trailing edges. Heat flux maximization did have some favorable consequences by increasing the turbine inlet temperature, but it provided no information about the engine performance loss caused by the bleeding of air from the compressor. It is a viable objective function only if it is decoupled from the aerodynamic and overall engine performance for closed-circuit cooling devices, for example.

### 2.1.3 Optimization of the engine cycle

An engine cycle analysis was implemented as a more realistic optimization objective function in order to take into account the effects of aerodynamic losses, fuel economy and internal cooling losses simultaneously with an increase in the turbine inlet temperature. One of two important performance parameters of a gas turbine engine will be optimized, either specific thrust (engine thrust force per linear momentum of engine air flow rate,  $\mathfrak{F}/\dot{m}v_\infty$ ), or thrust specific fuel consumption (mass flow rate of fuel per unit thrust,  $\dot{m}_f/\mathfrak{F}$ ). (Kerrebrock [31]).

$$F(V) = \frac{\mathfrak{F}}{\dot{m}v_\infty} = \sqrt{\left(\frac{T_{01}/T_1}{T_{01}/T_1 - 1}\right) \left( \frac{T_{0t}/T_1}{(T_{01}/T_1)\pi_c^{1-\frac{1}{\gamma}}} - 1 \right) \left( \pi_c^{1-\frac{1}{\gamma}} - 1 \right) + \frac{T_{0t}/T_1}{(T_{01}/T_1)\pi_c^{1-\frac{1}{\gamma}}} - 1} \quad (3)$$

$$F(V) = \frac{\dot{m}_f}{\mathfrak{F}} = \frac{c_p \left( T_{0t}/T_1 - (T_{01}/T_1)\pi_c^{1-\frac{1}{\gamma}} \right)}{Q_R \left( \frac{\mathfrak{F}}{\dot{m}} \right)} \quad (4)$$

Here,  $\dot{m}$  is the air mass flow rate,  $\dot{m}_f$  is the fuel mass flow rate,  $v_\infty$  is the flight speed,  $T_{0t}$  is the turbine inlet total temperature,  $T_{01}$  and  $T_1$  are the total and static temperatures at the engine inlet,  $Q_R$  is the heat value of the fuel, and  $\pi_c$  is the compressor stagnation pressure rise ratio. The optimum compressor pressure ratio for an ideal turbojet at maximum specific thrust can be found by differentiating specific thrust with respect to the compressor ratio [1].

$$\left(\pi_c^{1-1/\gamma}\right)_{\text{optimum}} = \frac{\sqrt{T_{0t}/T_1}}{T_{01}/T_1} \quad (5)$$

The real engine cycle analysis that has been used in our MCADO program includes losses associated with non-isentropic expansions and compressions in the diffuser, compressor, turbine and nozzle (Kerrebrock [31]; Brown et al. [3]). In addition to these frictional and diffusive losses, this analysis accounts for incomplete combustion and stagnation pressure losses in the burner. The working fluid is assumed to be a thermally perfect gas. Under- or over-expansion of the nozzle is ignored. In the case of turbo shafts and power generation turbines, the exhaust kinetic energy is also considered a loss. Much of these losses are aerodynamic and strongly depend upon flow deflection angle, ratio of blade chord to spacing and Reynolds number.

There are four main sources of loss in a turbine: internal cooling losses, profile losses due to shocks and boundary layers, secondary flow losses and tip leakage. The latter three are external aerodynamic losses, but the first influences turbine efficiency in three ways. First, the cooling air emerging from the blades increases the drag. Second, the cooling air suffers a pressure loss when passing through the cooling passages. Third, the transfer of heat from the hot gases to the cooling flow increases the entropy. The effect of cooling the turbine modifies the definition for the turbine efficiency. For turboshaft and high-bypass turbofan engines, the efficiency of internally cooled turbines is central to engine performance. Turbine efficiency has been defined as the ratio of the actual turbine work per unit of total air flow (primary plus cooling) divided by the ideal work that would be achieved by expanding that total airflow through the actual pressure ratio (Kerrebrock [31]).

$$\eta_{tt} = \frac{(1-f_c)(T_{04} - T_{05}) + f_c(T_{0c} - T_{05})}{[(1-f_c)T_{04} + f_c T_{0c}] \left[ 1 - (p_{05}/p_{04})^{\gamma_t-1/\gamma_t} \right]} \quad (6)$$

Here,  $T_{0c}$  is the stagnation temperature of the cooling air,  $T_{05}$  is the mean turbine exit temperature for the total flow,  $T_{04}$  is the mean turbine inlet stagnation temperature,  $p_{05}$  is the mean turbine exit stagnation pressure, and  $p_{04}$  is the mean turbine inlet stagnation pressure. The ratio of the coolant mass flow rate to total airflow rate is given by  $f_c$ .

Because cooling air is bled from the compressor, the power balance between the compressor and turbine must be modified by the work done by the turbine, as well as by the heat losses to the coolant. For a given temperature drop in the turbine and a closed-loop cooling system, the loss of heat to the coolant air reduces the amount of work that can be extracted. If the heated coolant air is injected and mixed with the hot combustion product gases and expanded to the turbine exit stagnation temperature,  $T_{05}$ , then the resulting shaft power is increased by the coolant ejection stagnation temperature,  $T_{0c}$ .

$$(\dot{m} - \dot{m}_c + \dot{m}_f)c_{pt}T_{04} + \dot{m}_c c_{pc}T_{0c} = (\dot{m} + \dot{m}_f)c_{pt}T_{05} + P_s \quad (7)$$

Here,  $P_s$  is the turbine temperature that lower rates result

## 2.2 Const

### 2.2.1 The

The prima turbine b) determini creep.

During constraint thermal li

Forced co temperature Because temperature perform temperature in the me at it from temperature reaches i

### 2.2.2 Cr

Creep is temperature the usefu metal te dimension Thus, th limiting



Here,  $P_s$  is the shaft power and  $c_{pt}$  and  $c_{pc}$  are the specific heat of the hot and coolant gases in the turbine, respectively. In this equation, the turbine exit temperature is dependent upon the temperature at the inlet to the coolant passages. This paradoxical effect is balanced by the fact that lower coolant temperatures allow higher turbine inlet temperatures and higher coolant flow rates result in higher internal pressure losses.

## 2.2 Constraint functions

### 2.2.1 Thermal integrity

The primary constraint on the optimization is concerned with the temperature limitation of the turbine blade material. The material temperature is also the most important factor in determining the failure modes caused by oxidation and sulfidation, and it is very important for creep.

During optimization, the material integrity of the turbine blade was maintained with a constraint that ensured that the maximum temperature in the metal did not exceed its material thermal limit.

$$G(V_i) = \frac{T_{\max}}{T_{\max}} - 1 < 0 \quad (8)$$

Forced convective heat transfer on the surface of the turbine blade makes the maximum temperature in the solid turbine blade,  $T_{\max}$ , a strong function of the turbine inlet temperature. Because we wish to maximize the turbine inlet temperature while keeping the maximum temperature in the metal below the limiting value, thermal integrity with optimum engine performance takes the form of an equality constraint. This constraint forces the maximum temperature in the metal blade to be equal to a user-specified value. For a given turbine inlet temperature, an optimal turbine cooling scheme is the one that keeps the maximum temperature in the metal blade at some limiting value with the least mass flow rate of the coolant. To look at it from the viewpoint of the constraints, for a given mass flow rate, the turbine inlet temperature should be increased to the point where the maximum temperature of the blade reaches its material limit.

### 2.2.2 Creep life

Creep is a plastic distortion of the airfoil shape over a long period of time and it is very temperature dependent. The combined effects of centrifugal stress and a high temperature limit the useful life of the blade. The temperature influence is so severe that a 20-degree change in metal temperature will typically change the life of the blade by a factor of two. For two-dimensional optimization, creep life can be estimated from the average metal temperature. Thus, the creep constraint was formulated to maintain average metal temperature below some limiting temperature that was based some a specified creep rate.

$$G(V_i) = \frac{\bar{T}}{T_{\max}} - 1 < 0 \quad (9)$$

For three-dimensional optimization, the highest stress occurs near the blade root, but the spanwise variation in gas temperature dictated a critical span for the prediction of creep life. The two-dimensional temperature field was analyzed at this critical span.

### 2.2.3 Thermo-mechanical fatigue

Thermo-mechanical fatigue, TMF, is the weakening of a material as it is subjected to repeated cyclic loading and temperature gradients. The cyclic thermal loads vary due to engine idle, take-off, cruise, descent and thrust reversal during daily engine operation. They are ignored for the purpose of this research. But, the thermal mismatch that causes strain in the metal due to steady temperature gradients has been incorporated into this design system via a two-dimensional thermo-elastic BEM analysis. Turbine durability limited by TMF was done with an equation similar to equation 1, but where the integrated thermal strains were minimized or maintained below a strain range,  $\delta_e$ .

$$G(\vec{V}) = \int_M (\epsilon_{TO}^T - \epsilon_{IDL}^T)^2 d\Omega < \delta_e \quad (10)$$

The development of these constraint functions required a computational aero-thermo-fluid analysis of the hot gas flow around the turbine blade iteratively coupled to the heat conduction in the solid blade, as well as to the heat transfer to the internal coolant fluid elements. Internally cooled turbine blade configurations were feasible whenever conditions (8) through (10) were satisfied, in addition to when the coolant air bleed pressure was high enough to drive the coolant flow and could also be accessed from the compressor.

### 2.2.4 Structural integrity

The centrifugal stress limitations were approximated with a simplified relation that assumed that the blade is a rotating thin bar with a tip radius  $R_t$ . The stress at some position  $R_i$  was calculated in terms of the centrifugal force acting on the mass,  $m$ , of the material. The elementary centrifugal force is  $dF = \rho \Omega^2 A r dr$ , where  $\rho$  is the density of the blade material and  $A$  is the local cross-sectional area of the blade. Centrifugal stress at the location  $R_i$  is then

$$\sigma_r(R_i) = \frac{F(R_i)}{A(R_i)} = \frac{\rho \Omega^2}{A(R_i)} \int_{R_i}^{R_t} A r dr \quad (11)$$

The result is that, for a given a fixed tip radius, blade root to tip distance, thickness of the coolant walls, thickness of the ribs and blade taper, the centrifugal stresses are set by the rotor speed. Thus, each two-dimensional section of the internally cooled turbine airfoils were designed such that their cross-sectional area was large enough to maintain the centrifugal load.

### 2.2.5 Vibratory fatigue

Aerodynamic forces are unsteady because the blades move past the wakes created by the upstream blades. They cause vibratory stresses that are usually not large, so long as the forcing frequency does not coincide with one of the natural frequencies of the blade. These frequencies can be avoided by assuming that the blade's principal moment of inertia,  $I$ , is

outsid  
constr

## 3 Nu

In the  
aerody  
gas flo  
equati  
turbine  
adiab  
attempt  
transfe  
results  
condu  
of the

In  
the tur  
and th  
alter s  
interac  
must b  
surface  
not kn

## 3.1 Co

The co  
condit  
heat co  
itself  
problem  
and nu  
flow c  
attracti

The  
obtaine  
compa

outside a particular range of resonant frequencies. Therefore, a single simple geometric constraint is required.

$$G(V_i) = \left| \frac{I}{\bar{I}} - 1 \right| > \varepsilon_I \quad (12)$$

### 3 Numerical aero-thermo-elastic analysis

In the old and all-too-frequent practise of computational modeling of turbomachinery blades, aerodynamic design engineers solve the system of fluid flow conservation equations in the hot gas flow region separately from the thermal design engineers who utilize the heat conduction equation within internally cooled turbine blades. The thermal boundary condition on the turbine blade exterior wall that is applied in the CFD analysis is usually a constant temperature, adiabatic heat flux condition, or an empirical wall temperature variation. If any coupling is attempted, it is usually done non-iteratively (directly) through the use of convection heat transfer coefficients. These are either estimated from some basic theory or taken mainly from results of experimental observations and then applied to the outer blade surface for the heat conduction analysis in the internally cooled turbine blade. Any further thermal-stress analysis of the blade is carried out afterwards.

In compressible flow situations, such as in a transonic turbine cascade, the temperature on the turbine blade wall will affect the velocity and pressure fields, especially the shock locations and the shape and size of the boundary layer. This modified gas thermodynamics may then alter slightly the temperature field in the turbine blade. Therefore, the mutual thermal interaction between the external hot gas flow-field and the heat conduction in the structure must be taken into account. In the realistic engineering environment, the wall temperatures and surface heat fluxes and the heat transfer coefficients on the turbine blade's external surface are not known in advance.

#### 3.1 Conjugate aero-thermal heat transfer

The conjugate heat transfer analysis allows one to avoid the specification of an unknown condition by resolving the temperature field within the hot gas stream simultaneously with the heat conduction in the turbine blade. An efficient conjugate heat transfer analysis can lend itself very nicely to the turbine cooling optimization problem. Conjugate heat transfer problems have been studied for many years. With the improvement of computer performance and numerical schemes, computational simulations of the Navier-Stokes equations for the fluid flow coupled with heat transfer in solid regions have become increasingly feasible. It is an attractive and marketable feature of contemporary CFD software.

The variation of the heat transfer coefficient on the outer surface of the turbine can be obtained from a computational thermal-fluid dynamics analysis where the following heat flux compatibility equation is used on the surface exposed to the hot combustion product gases.

$$-k_m \left( \frac{\partial T}{\partial n} \right)_m = k_g \left( \frac{\partial T}{\partial n} \right)_g \quad (13)$$

Here,  $k_m$  is the thermal conductivity of the outermost solid sub-domain (coating) and  $k_g$  refers to the thermal conductivity of external combustion product gases. The BEM heat conduction program and the finite volume CFD program were iteratively coupled with only a small number of iterations (9-12) between the two programs (Li & Kassab [32, 33]) needed in order to converge to a heat flux residual of less than  $1.0e-6$ .

In the conjugate procedure, the optimization program was started with a compressible CFD analysis of the turbine cascade using an unstructured finite volume Favre-averaged Navier-Stokes solver (Han and Liu [34]) or a structured finite differencing Reynolds-averaged Navier-Stokes solver (Chima [35]). The former code used the two-equation  $k$ -epsilon turbulence model, while the algebraic Baldwin-Lomax model was used for the latter. The CFD solver was given an initial guess for the temperature distribution,  $T_0$ , on the turbine blade surface. It also required the turbine inlet static temperature,  $T_{inlet}$ , inlet static pressure,  $p_{inlet}$ , back pressure,  $p_{exit}$ , inlet Mach number,  $M_{inlet}$ , and inlet flow angle, for its boundary conditions.

Once converged, the flow-field analysis code computed turbulent heat fluxes,  $Q_0$ , that were applied as thermal boundary conditions directly to the BEM code analyzing heat conduction inside the blade material. After converging on the heat flux dependent boundary conditions of the coolant passages,  $T_{cool}(Q)$ , a new temperature distribution was obtained on the exterior blade surface. Since this wall temperature variation was, in general, different from the wall temperatures specified to the hot gas flow-field analysis code, it was applied as a thermal boundary condition again to the CFD code. Another CFD solution then computed new corresponding heat fluxes on the blade exterior surface. This process was repeated several times until the heat fluxes converged. Thereafter, for fixed outer turbine blade shape, heat transfer coefficients on the outer turbine airfoil boundary were computed from the converged hot surface temperatures and fluxes and the corresponding turbine inlet total temperature,  $h_0 = Q_0 / (T_0 - T_{0inlet})$ . The convective heat transfer coefficient distribution then remained fixed during the entire optimization of the coolant passage geometry, or it was intermittently updated after the design was significantly modified.

### 3.2 Non-linear heat conduction

The conduction of heat within the solid turbine blade was modeled by the steady state, non-linear, partial differential equation.

$$\nabla \cdot (k_m(T) \nabla T) = 0 \quad (14)$$

Here,  $k_m(T)$  is the temperature-dependent coefficient of thermal conductivity and  $T$  is the temperature. The computational domain was divided into a finite number of sub-domains ( $m = 1, \dots, ndom$ ) where the material properties within each sub-domain varied continuously, homogeneously, and isotropically. This equation was numerically solved by means of the boundary element method (Brebba [36]).

The boundaries of two-dimensional domains were discretized with  $N_{BE}$  linear isoparametric boundary elements connected at their endpoints between  $N_{BN}$  boundary nodes. Three-dimensional surfaces were discretized with quadrilateral boundary elements. These elements were numerically integrated using Gaussian quadrature. A self-adaptive cubic local coordinate transformation was used for the singular and near singular boundary elements (Telles [37]). The resulting system of algebraic equations was expressed in matrix form, with  $\{T\}$  and  $\{Q\}$  being the vectors of nodal temperatures and fluxes.

In  
blade

Here,  
blade,  
variati

3.2.1  
The h  
functi  
depen  
tempe  
Kirchl

Here,  
variati  
form e

Linear

Kirchl

Invers

Kir  
into L  
transfo  
temper  
 $\bar{Q} = -$   
solutio  
depend  
linear  
derivat

$$[\mathbf{H}]\{\mathbf{T}\} = [\mathbf{G}]\{\mathbf{Q}\} \quad (15)$$

In the conjugate aero-thermal shape optimization problem, the outer surface of the turbine blade was subjected to forced convection heating.

$$Q = -k \frac{\partial T}{\partial n} = h_0 (T_0 - T_{0\text{inlet}}) \quad (16)$$

Here,  $h_0$  is the convection heat transfer coefficient that varied along the surface of the turbine blade, and  $T_{0\text{inlet}}$  is the turbine inlet total temperature. This temperature was used as a design variable in the numerical optimization procedure.

### 3.2.1 Temperature-dependent thermal conductivity

The heat conduction problem was linear if the coefficient of thermal conductivity was not a function of temperature and when the boundary conditions were either constant or linearly dependent on the temperature or heat flux. When the coefficient of thermal conductivity was temperature-dependent, the heat conduction equation was linearized by the application of Kirchhoff's transformation that defined the heat function,  $u$ , as follows.

$$u = \int_0^T \frac{k(T)}{k_0} dT \quad \nabla u = \frac{k(T)}{k_0} \nabla T \quad (17)$$

Here,  $k_0$  was the reference coefficient of thermal conductivity. The linear temperature variation of thermal conductivity, along with its associated Kirchhoff's transform, and a closed-form expression for the inverse transforms, are given below.

$$\text{Linear Variation} \quad k = k_0 [1 + \beta(T - T_0)] \quad (18)$$

$$\text{Kirchhoff's Transform} \quad u = (1 - \beta T_0)T + \frac{1}{2}\beta T^2 \quad (19)$$

$$\text{Inverse Transform} \quad T = \frac{-(1 - \beta T_0) + \sqrt{(1 - \beta T_0)^2 + 2\beta u}}{\beta} \quad (20)$$

Kirchhoff's transformation converts the governing steady-state heat conduction equation into Laplace's equation for the heat function,  $\nabla^2 u = 0$ . Dirichlet boundary conditions were transformed to heat functions by applying Kirchhoff's transformation directly to the known temperature values. Neumann boundary conditions were linearly related to the heat flux,  $\bar{Q} = -k \partial T / \partial n = -k_0 \partial u / \partial n$ . Convective heat transfer coefficients were applied directly to the solution of the BEM system matrix whenever the thermal conductivity was not temperature-dependent. In the case of a convective heat transfer boundary condition, the heat flux was a linear function of temperature. That relationship was solved for the normal temperature derivative and substituted into the BEM system of algebraic equations. The coefficients of the

unknown temperatures were then assembled into the unknown coefficient matrix and factored with the other nodal temperatures appearing on the left-hand side of the BEM equation set.

When the conductivity was temperature-dependent, or when the heat transfer coefficients,  $h$ , were a function of temperature, or when the ambient (bulk) temperatures ( $T_{\text{amb}}$ ,  $T_{\text{inlet}}$ ,  $T_{\text{cool}}$ ) were dependent on the heat flux, or in any other case when the function  $Q(T)$  was not linear, an iterative procedure was required. For example, when a convection heat transfer boundary condition appeared with a temperature-dependent conductivity, the flux boundary condition became the following non-linear expression for  $u$ .

$$\bar{Q}(u) = -k_0 \frac{\partial u}{\partial n} = \frac{h}{\beta} \sqrt{(1 - \beta T_0)^2 + 2\beta u} - \frac{h(1 - \beta T_0)}{\beta} - hT_{\text{amb}} \quad (21)$$

The Newton-Raphson (N-R) scheme was employed to deal with the non-linearity because it offered stability and its quadratic convergence properties allowed it to converge in only a couple of iterations. The implementation of the N-R approach on the BEM matrix set was very similar to the algebraic manipulations detailed previously. Although the BEM matrices  $[H]$  and  $[G]$  needed to be integrated only once, this scheme required that the BEM solution matrix be factored every iteration. The N-R Jacobians were easily computed because the BEM coefficient matrices were constant. The Jacobian of the flux boundary condition for  $h$  was found by taking the derivative with respect to the Kirchhoff's heat function.

$$\left( \frac{\partial Q}{\partial u} \right)^{n-1} = \frac{h}{\sqrt{(1 - \beta T_0)^2 + 2\beta u^{n-1}}} \quad (22)$$

The superscript  $n$  indicates the iterative counter. The Jacobians of the N-R scheme were evaluated at the previous iteration  $n-1$ . The iterative N-R scheme required an initial guess as to the boundary temperatures.

### 3.2.2 Multiple regions with temperature-dependent thermal conductivity

For the multi-component turbine blade geometry, the heat-conducting solid was composed of more than one material sub-domain where each material had a different coefficient of thermal conductivity that was also temperature-dependent. This problem was formulated using Kirchhoff's transformation. The compatibility relations at the interface between the two neighboring materials coupled different Kirchhoff's heat functions. The compatibility relations for temperature and flux when using Kirchhoff's transformation at the interface between regions 1 and 2 were derived for the linear and exponential representations.

$$\frac{-(1 - \beta_1 T_{01}) + \sqrt{(1 - \beta_1 T_{01})^2 + 2\beta_1 u_1}}{\beta_1} = \frac{-(1 - \beta_2 T_{02}) + \sqrt{(1 - \beta_2 T_{02})^2 + 2\beta_2 u_2}}{\beta_2} \quad (23)$$

$$-\left( k_{01} \frac{\partial u}{\partial n} \right)_1 = \left( k_{02} \frac{\partial u}{\partial n} \right)_2 \quad (24)$$

Since  
funct  
in the  
solve

The  
condi

A dif  
the Ja

3.2.3  
Beca  
was a  
the se  
elem  
coord  
was c  
this p  
bound

Ev  
equat  
probl  
thin c  
infini  
soluti  
of the  
therm  
produ  
only c

3.3 F

The s  
cool  
flow  
transf

Since the compatibility relation for temperature did not yield a linear relationship for the heat function  $u$ , an iterative N-R procedure was utilized. First, the heat function  $u_1$  was factored as in the BEM matrix formulation. Then, the linear law temperature compatibility relation was solved for the heat function  $u_2$ .

$$u_2 = \frac{\left[ (1 - \beta_2 T_{02}) - \frac{\beta_2}{\beta_1} (1 - \beta_1 T_{01}) + \frac{\beta_2}{\beta_1} \sqrt{(1 - \beta_1 T_{01})^2 + 2\beta_1 u_1} \right]^2 - (1 - \beta_2 T_{02})^2}{2\beta_2} \quad (25)$$

The Jacobian of the Newton-Raphson scheme for the linear temperature variation of thermal conductivity was then derived.

$$\left( \frac{\partial u_2}{\partial u_1} \right)^{n-1} = \frac{\left[ (1 - \beta_2 T_{02}) - \frac{\beta_2}{\beta_1} (1 - \beta_1 T_{01}) + \frac{\beta_2}{\beta_1} \sqrt{(1 - \beta_1 T_{01})^2 + 2\beta_1 u_1^{n-1}} \right]}{\sqrt{(1 - \beta_1 T_{01})^2 + 2\beta_1 u_1^{n-1}}} \quad (26)$$

A difficulty arose when more than one region was connected to a single node. In these cases, the Jacobian was related to the heat function of a single region.

### 3.2.3 Thermal barrier coatings

Because a realistic thermal barrier coating is very thin (75 – 200 microns), a special concern was addressed when integrating over near singular boundary elements. If the distance between the source coordinate and the boundary element of integration was less than the length of the element, a self-adaptive cubic variable transformation (Telles [37]) was employed. The coordinate nearest to the singularity in the localized boundary integration coordinate system was determined algebraically, and the Jacobian of the cubic transformation was set to zero at this point. Using this approach, the number of Gaussian quadrature points needed for accurate boundary integration was reduced.

Even with an accurate integration of nearly singular boundary elements, the system of equations became more ill conditioned as the thickness of the coating was reduced. This problem has already been addressed by the dual boundary element (DBEM) formulation for thin cracks (Aliabadi & Mellings [38]). Because the DBEM was specifically designed for infinitesimally thin cracks, the problem of very thin domains was alleviated with the proper solution to the ill-conditioned system of equations. The singular value decomposition (SVD) of the coefficient matrix  $[A]$  allowed for a greatly improved solution in cases with very thin thermal barrier coatings and thin coolant walls. Solutions with an error of less than 1% were produced even when the thickness of the coating was less than 0.00001 times the chord. The only drawback was the longer computing time required for factoring the matrix with the SVD.

### 3.3 Forced convection correlations for internal heat transfer

The specification of convective heat transfer coefficients and bulk fluid temperatures of the coolant fluid resolved the application of thermal boundary conditions on the internal coolant flow passage surfaces. Semi-empirical correlations were used to determine the coolant heat transfer coefficients,  $h_{cool,n}$ , and the bulk coolant temperatures,  $T_{cool,n}$ , for each  $n$ th coolant

passage. They were assumed to vary only in the radial direction (from the root to tip sections) and between the coolant passages.

Appropriate to the physical phenomenon of forced convection, the heat transfer coefficient,  $h_{\text{cool}}$ , could vary with respect to a large number of parameters (White [39]). This variation was expressed as a function of the following: stream-wise velocity of the coolant air,  $w$ , coolant air density,  $\rho_{\text{cool}}$ , hydraulic diameter of the coolant passage,  $D_h$ , temperature of the wall,  $T_w$ , ambient coolant temperature,  $T_{\text{cool}}$ , wall roughness,  $\epsilon$ , temperature-dependency of the fluid properties,  $\mu$ ,  $k$ ,  $c_p$ , Coriolis acceleration due to rotor speed,  $2\bar{\Omega} \times \bar{w}$ , the thermal buoyancy due to centrifugal pressure gradient,  $\Omega^2 R \beta$ , and the geometric shape.

$$h_{\text{cool}} = f(\bar{w}, \rho_{\text{cool}}, D_h, T_w, T_{\text{cool}}, \epsilon, \mu, k, c_p, g\beta, 2\bar{\Omega} \times \bar{w}, \text{shape}) \quad (27)$$

Assumptions have been made in order to simplify this function and to arrive at a usable relationship. The temperature differences in the coolant were assumed to be small enough to eliminate the temperature-dependency of physical properties. Thermal buoyancy and Coriolis forces were neglected. Because the internal coolant passages do not, in general, have circular cross-sections, the heat transfer correlations were based on the hydraulic diameter of the coolant passages,  $D_h = 4A_n/P_n$ , where  $P_n$  was the wetted perimeter of the  $n$ th coolant flow passage. The coolant mass flow rate,  $\dot{m} = \rho_{\text{cool}} A w$ , was specified as a boundary condition, and  $A$  is the effective cross-sectional area of the coolant passage. It was often the most important design variable during the numerical optimization process. In fact, the minimization of the coolant flow rate is a very desirable objective of any coolant scheme, but it could not be explicitly minimized because of its independence as a boundary condition.

In an effort to enhance heat transfer, modern internal cooling designs utilize turbulators such as trip strips and transverse ribs in order to increase the heat transfer coefficients. These devices induce early transition to turbulence and greatly increase the pressure losses, while moderately increasing the convective heat transfer (White [39]). Results of experimental data for simplified forced convection heat transfer are quite common in the open literature. Correlations for rough tubes, such as those containing trip strips, are rather sparse. The effect of placing trip strips in the coolant passages as a design variable was simulated with wall roughness, using an analogy between skin friction and boundary layer heat transfer.

### 3.3.1 Heat and momentum similarity

The Reynolds analogy provided a relationship between the wall shear stress and the heat transfer.

$$St = \frac{f/8}{1 + 12.7(Pr^{2/3} - 1)\sqrt{f/8}} \quad (28)$$

Here, the Stanton number,  $St = h_{\text{cool}}/\rho_{\text{cool}}c_p w$ , and the friction factor,  $f = 8\tau_w/\rho_{\text{cool}}w^2$ , were based on the bulk properties of the cooling fluid. The value of the friction factor could be taken from the well-known Moody chart, knowing the relative roughness ratio,  $\epsilon/D_h$ , and the Reynolds number (Holman [40]). For optimization purposes, the friction factor will change during the numerical optimization process. Therefore, an explicit formula given by Haaland was used (White [39]).

This e  
+/-15%  
range  
of eac  
specifi  
Th  
correl  
roughe  
in con  
groove  
( $\epsilon_p/\epsilon$ )  
Law"  
grain (  
the rou  
flow a

Con  
lamina  
line at  
rough  
data. ?  
Dip  
transfe  
(Webb  
equatic  
friction

The ex  
differen  
similar  
correla  
0.045.  
a range



$$\frac{1}{\sqrt{f}} = -1.8 \log \left[ \frac{6.9}{Re_D} + \left( \frac{\epsilon/D_h}{3.7} \right)^{1.11} \right] \quad (29)$$

This explicit expression is accurate to within 2% of the Moody chart, which itself is accurate to +/-15% versus experimental data for fully turbulent flows having Reynolds numbers in the range  $10^3 < Re < 10^8$ . During the numerical optimization procedure, the wall roughness heights of each coolant passage were independent design variables ranging from 0 up to a user-specified limit around 0.1.

The Reynolds analogy is adequate only for uniform fully rough walls, but more rigorous correlations are needed to predict the friction and heat transfer characteristics of other roughened surfaces. Webb [41] has categorized the many possible roughness geometries used in commercial applications into three basic roughness families: uniform, repeated ribs and grooves. The key dimensionless variables are the roughness ratio ( $\epsilon/D_h$ ), the roughness spacing ( $\epsilon_p/\epsilon$ ) the rib width ( $\epsilon_w/\epsilon$ ) and the shape of the roughness element. The "Friction Similarity Law" was developed by Nikuradse and described by Schlichting [42] for closely packed sand grain (uniform) roughness. The velocity profile, based on the "Law of the Wall" depends on the roughness Reynolds number,  $e^+$ , and is obtained by integrating the velocity profile over the flow area.

$$\sqrt{\frac{8}{f}} = -2.5 \ln \left( \frac{2\epsilon}{D_h} \right) - 3.75 + B(e^+) \quad e^+ = \frac{\epsilon}{D_h} Re_D \sqrt{\frac{f}{8}} \quad (30)$$

Correlations have shown that the friction factor approaches the smooth tube value in the laminar regime. In the turbulent regime, the smaller  $\epsilon/D_h$  values drift above the smooth tube line at higher Reynolds numbers and attain an asymptotic constant value that is termed the fully rough condition (eqn 35). The function  $B(e^+)$  was obtained via curve fitting of Nikuradse's data. The friction factor variation versus Reynolds number is shown in Figure 4.

Dipprey and Sabersky [43] developed a rational correlation based on the heat momentum transfer analogy for rough surfaces. It is applicable to any geometrically similar roughness (Webb [41]). The correlating function is obtained by integrating the momentum and energy equations over the boundary layer thickness. The Stanton number was here a function of the friction factor, Prandtl number  $Pr$ , and the functions  $G(e^+)$  and  $B(e^+)$ .

$$St = \frac{f/8}{1 + \sqrt{f/8} [G(e^+) Pr^\phi - B(e^+)]} \quad (31)$$

The exponent  $\phi$  is 0.44 for sand grain and 0.57 for transverse ribs. The  $G(e^+)$  and  $B(e^+)$  are different for the different roughness families. Webb [41] applied the model to geometrically similar transverse rib roughness where  $\epsilon_p/\epsilon = 10, 20$  and 40. The heat transfer similarity law correlated with the experimental data through a range of roughness ratios between 0.01 and 0.045. Figure 5 illustrates the Stanton number correlations for various roughness families over a range of roughness ratios at  $Re = 10,000$ .

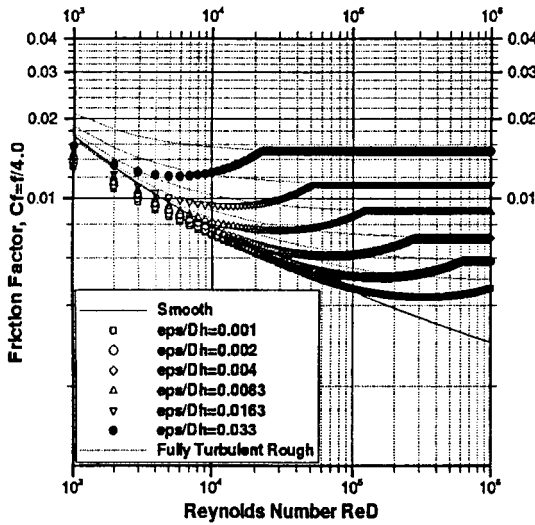


Figure 4: Friction factor correlations for roughened tubes.

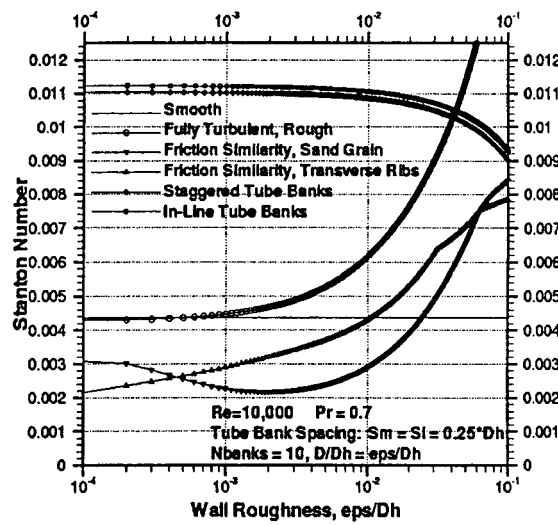


Figure 5: Correlations for Stanton number over a range of wall roughness ratios.

### 3.3.2 Banks of pin fins and turning bends

The trailing edge coolant flow passages often have multiple rows of heat exchanging pin fins called pedestal cooling schemes. The pressure drop for the flow through a bank of pin fins having 10 or more rows was expressed as follows (Holman [40]).

$$\Delta p_{\text{cool}} = \left( \frac{w_{\text{max}}}{w} \right)^2 2f' N_{\text{banks}} \left( \frac{\mu_w}{\mu_{\text{cool}}} \right)^{0.14} \quad (32)$$

Here,  $w_{\text{max}}$  is the coolant speed at minimum flow area and  $N_{\text{banks}}$  is the number of transverse rows. The empirical friction factor was given by Jakob (Holman [40]) for staggered tube and in-line arrangements, respectively.

$$f' = \left\{ 0.25 + \frac{0.118}{[(S_n - D)/D]^{1.08}} \right\} \text{Re}_{\text{max}}^{-0.16} \quad (33)$$

$$f' = \left\{ 0.044 + \frac{0.08 \frac{S_p}{D}}{[(S_n - D)/D]^{0.43 + 1.13D/S_p}} \right\} \text{Re}_{\text{max}}^{-0.15} \quad (34)$$

Most internal cooling schemes have serpentine passages that cause the coolant air to undergo sharp turns so that it can flow radially outward towards the tip of the blade and radially inward towards the root several times. Therefore, the pressure losses in the coolant passages included those associated with 180° flow turning bends by the following empirical formula proportional to the dynamic pressure (White [39]).

### 3.3.3

The st  
rotation  
pressu  
flow t  
each c  
ending  
losses  
After  
elemen  
assembl  
iterativ  
 $T_{t,\text{cool}}$

Th  
total p  
equatio  
coolan  
compre  
coolan  
elemen  
BEM  
provid  
compu

### 3.4 Th

This m  
solver  
therma  
deform  
turbine  
the turl

The  
relation  
orienta  
defined  
the foll

where  
Equilib

$$\Delta p_{\text{turn}} = \left( \frac{1}{2} \rho w^2 \right) R_K \quad R_K = \frac{0.4}{(36.37 D_h)^{0.2}} \quad (35)$$

### 3.3.3 One-dimensional fluid elements for internal coolant flow modeling

The steady state, quasi-one-dimensional, compressible system of Navier-Stokes equations with rotation, heat addition and friction (Saad [44]) was used to determine the bulk temperatures and pressure losses within the serpentine coolant passages. The streamwise direction of the internal flow began at the inlet at the root of the leading edge passage, followed along the length of each coolant passage in the serpentine, past 180° turning bends, around the struts and finally ending at the trailing edge ejection slot. The wall shear stress and 180° turning bend pressure losses were functions derived from empirical correlations presented in the previous section. After discretizing the streamwise direction into a finite number of fluid elements, the local element momentum (pressure loss), element rothalpy and nodal continuity equations were assembled into a global matrix form using the finite element method. This system was iteratively solved for the coolant flow rate,  $G_{\text{cool}}$ , total pressure,  $p_{t,\text{cool}}$ , and total temperature,  $T_{t,\text{cool}}$ .

Three boundary conditions were applied to the fluid element system: the coolant supply total pressure, the static pressure at the trailing edge ejection and the adiabatic compression equation. The latter condition replaced the specification of total temperature at the inlet to the coolant passages. This was used because the coolant was assumed to bleed from the compressor, so the total temperature was coupled to the total pressure at the inlet. The bulk coolant temperature drop across each element was dependent upon the heat addition to the element. This heat addition was calculated from the integrated the heat flux computed by the BEM heat conduction code. Subsequent solutions to the conjugate heat transfer problem provided better estimates of the heat flux, and the iterative scheme proceeded until the computed heat fluxes converged to within a reasonable residual.

### 3.4 Thermo-elasticity

This multi-disciplinary research effort continued with the integration of a static thermo-elastic solver using the BEM. The resulting thermal loads in the turbine blade predicted by the aero-thermal program were submitted to the thermo-elastic solver for a development of the deformation and stress fields in the turbine blade. This inter-disciplinary coupling provides a turbine designer with a tool for confidently expanding the limits and improving performance of the turbine cooling scheme.

The governing partial differential equations of elasto-statics assume that there is a linear relationship between the stress and the strain response. It also neglects any changes in the orientation of the body due to displacements. The two-dimensional state of stress at a point is defined using a second-order symmetric stress tensor  $\sigma_{ij}$ . These stress components must satisfy the following equilibrium equations throughout the interior of the solid body,

$$\frac{\partial \sigma_{ij}}{\partial x_j} + b_k = 0 \quad (36)$$

where  $b_k$  are the net body forces per unit volume necessary to keep the body in equilibrium. Equilibrium on the boundary requires that  $p_k = \sigma_{kj} n_j$ , where  $n_k$  is the unit outward normal

vector to the surface  $\Gamma$ . The state of strain at a point within the solid is denoted by the second-order symmetric strain tensor,  $\epsilon_{ij}$ . The states of stress and strain for an isotropic solid body are related through the stress-strain relations, also known as Hooke's Law, which depend on the material behavior. Thermo-elastic effects, which involve dilatation or contraction due to changes in temperature, can be included as initial stresses,  $\sigma_{ij}^0$ . The initial stresses for a thermally isotropic material can be added to the stress-strain relation.

$$\sigma_{ij} = \lambda \delta_{ij} \frac{\partial u_k}{\partial x_k} + \mu \left( \frac{\partial u_i}{\partial x_j} + \frac{\partial u_j}{\partial x_i} \right) - \lambda \beta (T - T_0) \delta_{ij} \quad (37)$$

Here,  $u_k$  is the vector displacement field,  $\delta_{ij}$  is the Kronecker delta symbol,  $\mu$  is the shear modulus,  $\lambda$  is Lamé's constant,  $\beta$  is the thermal expansion coefficient,  $T$  is the temperature, and  $T_0$  is the reference temperature.

The BEM has been found to be an effective solution strategy of the Navier-Cauchy equation and thermo-elasticity (Rizzo & Shippy [45]). The initial stress term can be used to deal with thermal expansion and other non-linear effects such as plasticity (Brebbia & Dominguez [46]). The result is the boundary/domain integral equation for static thermo-elasticity problems with body forces. In this equation, the initial stress field and body forces remain as domain integrals.

$$c_{\ell k}(\bar{x}) u_k(\bar{x}) + \int_{\Gamma} p_{\ell k}^* u_k d\Gamma = \int_{\Gamma} u_{\ell k}^* p_k d\Gamma + \int_{\Omega} u_{\ell k}^* b_k d\Omega - \int_{\Omega} \epsilon_{\ell j k}^* \lambda \beta (T - T_0) \delta_{jk} d\Omega \quad (38)$$

In order to avoid the need for an internal mesh and to preserve the boundary-only nature of the BEM, the domain integrals can be transformed into boundary (surface) integrals. The first implementation of the use of the divergence theorem to transform body-loading effects into boundary integrals was presented by Cruse [47]. Rizzo and Shippy [45] presented a similar approach for thermo-elastic problems that could be easily adapted to gravitational and centrifugal loading by expressing the body forces as a differential of a scalar potential function  $\nabla \psi = \bar{\Omega} \times (\bar{\Omega} \times \bar{R})$ . The potential function satisfies the following harmonic relationship with  $\Psi_0$  a constant defined by  $\nabla^2 \psi = \Psi_0$ .

The body force integral was integrated by parts and the divergence theorem was applied to transform one domain integral to a boundary integral (Brebbia & Dominguez [46]). After applying the definition of the Galerkin vector, the following expression was obtained for the body force integral:

$$\int_{\Omega} u_{\ell k}^* b_k d\Omega = \int_{\Gamma} U_{n\ell}^* \psi d\Gamma + \frac{1-2\nu}{2(1-\nu)} \left\{ \int_{\Gamma} U_{\ell}^* \frac{\partial \psi}{\partial n} d\Gamma - \int_{\Gamma} P_{\ell}^* \psi d\Gamma - \Psi_0 \int_{\Gamma} G_{n\ell}^* d\Gamma \right\} \quad (39)$$

The thermo-elastic effects can be presented in a similar fashion. The initial stress term is equivalent to adding a body force equal to  $(-\gamma \partial(T - T_0)/\partial x_k)$ . The Galerkin fundamental solution is then differentiated three times. The resulting thermo-elastic kernels are identical to two of the body force boundary kernels.

where  
numeri  
be writ

The v  
bound  
bound  
matric  
matric  
passed  
by inv  
singula  
turbine  
conditi

#### 4 Imp

The p  
conduc  
heat ra  
a par  
coeffic  
inverse  
operati

In g  
analyti  
direct  
In the  
differe  
referre  
concep  
sensitiv  
only th  
variabl  
adjoint  
fluxes)  
compli  
each of  
discret  
differe

$$\int_{\Omega} \varepsilon_{ijk}^* \lambda \beta (T - T_0) \delta_{jk} d\Omega = \frac{(1-2\nu)\gamma}{2(1-\nu)} \left\{ \int_{\Gamma} P_i^* (T - T_0) d\Gamma - \int_{\Gamma} U_i^* \frac{\partial T}{\partial n} d\Gamma \right\} \quad (40)$$

where  $\nu$  is the Poisson's ratio. After the application of boundary element discretization and numerical integration of the integrands, the BEM system of equations for thermo-elasticity can be written in matrix form as follows.

$$[H_E]\{U\} = [G_E]\{P\} + [D_n]\{\Psi\} + \frac{1-2\nu}{2(1-\nu)} \left\{ [G_g] \left\{ \frac{\partial \Psi}{\partial n} - \gamma Q \right\} - [H_h]\{\Psi - \gamma(T - T_0)\} - [E_n]\Psi_0 \right\} \quad (41)$$

The vectors  $\{U\}$  and  $\{P\}$  represent the values of the displacements and tractions at the boundary nodal locations. The centrifugal potential function,  $\{\Psi\}$ , temperatures,  $\{T\}$ , and boundary heat fluxes,  $\{Q\}$ , are known, and can be multiplied by their respective coefficient matrices. The application of boundary conditions allows the columns of the  $[H_E]$  and  $[G_E]$  matrices to be multiplied by the known displacements and tractions, while the unknowns are passed into a vector  $\{X\}$ . The result is a system of equations,  $[A]\{X\} = \{F\}$ , that can be solved by inverting the coefficient matrix  $[A]$  with Gaussian elimination, LU decomposition, or singular value decomposition (SVD) (Press et al. [21]). The latter solver is necessary for turbine blades with extremely thin coolant walls and thermal barrier coatings that create ill-conditioned matrices.

#### 4 Implicit BEM design sensitivity

The partial derivatives of field variables (temperatures, temperature gradients, thermal conductivity, heat sources, etc.) and boundary values (heat fluxes, heat transfer coefficients, heat radiation, etc.) with respect to the set of design variables are very useful when performing a parametric study of a particular design. These partial derivatives are called design sensitivity coefficients. The implementation of gradient-based numerical optimization algorithms for inverse thermal shape design and optimization require these partial derivatives as part of their operation.

In general, there are four methods that can be used to determine sensitivity coefficients: 1) analytical differentiation, 2) numerical differentiation of the solution by finite differences, 3) direct implicit differentiation of the governing equations, and 4) the adjoint variable method. In the arena of modern applied numerical methods and computational fluid dynamics, analytic differentiation of the governing equations is generally impossible. The fourth method has been referred to as the adjoint variable method or the continuum approach. It uses variational concepts such as the material derivative (Meric [48]). By defining an adjoint problem, the sensitivity coefficients are found in terms of the primary and adjoint variables, thus requiring only the solution of one adjoint system to obtain the gradient with respect to every design variable. Although it has been proven successful with finite elements, the BEM version of the adjoint variable method was less satisfactory because the approximate adjoint tractions (or fluxes) could not be specified uniquely. The adjoint variable method requires a very complicated formulation of the optimization problem that needs to be developed uniquely for each objective function. Due to this fact, as well as to its overall decreased accuracy versus discretized differentiation, only the second and third methods, finite differencing and implicit differentiation have been incorporated into this research.

The second method, finite differencing, is the simplest, most common and most expensive strategy for obtaining sensitivity coefficients. It requires the brute force solution of the governing system discretized by the BEM once for every design variable for first-order forward differencing formulas.

$$\frac{\partial F}{\partial V_i} = \frac{F(V_i + \Delta V_i) - F(V_i)}{\Delta V_i} \quad (42)$$

If second-order accuracy is desired, the governing system must be evaluated twice per every design variable for central differencing. The finite differencing method for sensitivity calculations can be prohibitively expensive, especially when the design study or optimization concerns complex three-dimensional problems.

The third method involves the implicit differentiation of the equations at the system level (Hafka & Malkus [49]). Considerable effort has been applied to these techniques and they have been used extensively for the efficient implementation of shape optimization of large-scale structures. Implicit differentiation offers a practical design sensitivity calculation, because the factorization of coefficient matrices needs to be performed only once and stored. In addition, they have been found to be more accurate than finite differences (Aliabadi & Mellings [38]). Kane and Saigal [50] obtained their sensitivity coefficients by the implicit differentiation of the coefficient matrices formed by the boundary integral equations of two-dimensional sub-structural problems. This method has been extended to three-dimensional elasticity problems (Yamazaki et al. [51]).

#### 4.1 Implicit differentiation for thermal design sensitivity coefficients

The system of boundary integral equations was differentiated with respect to the vector of design variables,  $V_i$ .

$$\begin{aligned} \frac{\partial c(x)}{\partial V_i} T(x) + c(x) \frac{\partial T(x)}{\partial V_i} + \int_{-1}^1 \frac{\partial q^*(x, \xi)}{\partial V_i} T(\xi) |\bar{\eta}| d\xi + \int_{-1}^1 q^*(x, \xi) \frac{\partial T(\xi)}{\partial V_i} |\bar{\eta}| d\xi + \int_{-1}^1 q^*(x, \xi) T(\xi) \frac{\partial |\bar{\eta}|}{\partial V_i} d\xi \\ = \int_{-1}^1 \frac{\partial u^*(x, \xi)}{\partial V_i} q(\xi) |\bar{\eta}| d\xi + \int_{-1}^1 u^*(x, \xi) \frac{\partial q(\xi)}{\partial V_i} |\bar{\eta}| d\xi + \int_{-1}^1 u^*(x, \xi) q(\xi) \frac{\partial |\bar{\eta}|}{\partial V_i} d\xi \end{aligned} \quad (43)$$

The derivatives of the boundary conditions were found in the same way.

$$\text{Dirichlet} \quad \overline{\frac{\partial T}{\partial V_i}} = 0 \quad (44)$$

$$\text{Neumann} \quad \overline{\frac{\partial q}{\partial V_i}} = 0 \quad (45)$$

$$\text{Robin} \quad -k \frac{\partial q}{\partial V_i} - \frac{\partial k(T)}{\partial T} \frac{\partial T}{\partial V_i} q = \frac{\partial h}{\partial V_i} (T - T_{\text{amb}}) + h \left( \frac{\partial T}{\partial V_i} - \frac{\partial T_{\text{amb}}}{\partial V_i} \right) \quad (46)$$

After d  
system

The  
and [H  
fundam  
spatial

Unfortu  
(1/r<sup>2</sup>)  
resulting  
compute  
but, in  
somewh  
the sing  
problem  
consum  
fundam  
three tir  
surfaces  
closed-f  
In th  
slightly  
[dH/dV]

The bou  
advanta  
because  
time is  
integrati  
computa  
matrices  
Impli  
because  
The line  
and flux  
from the

After discretization, but before the application of boundary conditions, the linear algebraic system can be expressed in the following form.

$$[\partial \mathbf{H} / \partial \mathbf{V}]\{\mathbf{T}\} + [\mathbf{H}]\{\partial \mathbf{T} / \partial \mathbf{V}\} = [\partial \mathbf{G} / \partial \mathbf{V}]\{\mathbf{Q}\} + [\mathbf{G}]\{\partial \mathbf{Q} / \partial \mathbf{V}\} \quad (47)$$

There are two possible ways of determining the differentiated coefficient matrices,  $[\mathbf{C}]$ ,  $[\mathbf{G}]$  and  $[\mathbf{H}]$ . In most BEM implicit differentiation methodologies, the derivatives of the fundamental solution that appear in the preceding equation are calculated implicitly from the spatial derivative in the  $\bar{\mathbf{x}}$  and  $\bar{\xi}$  coordinate systems (Yamazaki et al. [51]).

$$\frac{\partial u^*}{\partial V_i} = \frac{\partial u^*}{\partial x_m} \left( \frac{\partial x_m}{\partial V_i} - \frac{\partial \xi_m}{\partial V_i} \right) \quad (48)$$

Unfortunately, these integrands result in singular fundamental solutions of the order  $(1/r)$  and  $(1/r^2)$  in two-dimensional problems, and  $(1/r^2)$  and  $(1/r^3)$  in three-dimensional problems, resulting in the need for hyper-singular integration. The rigid body assumption can be used to compute some weakly singular integrals that occur when the source and field points coincide, but, in general special methods are needed. Hyper-singular integration techniques are somewhat complex, requiring Laurent series expansions of the hyper-singular integrand about the singular point and a transformation to a local polar coordinate system in three-dimensional problems (Guiggiani et al. [52]). Although hyper-singular integration is complex and time-consuming, the savings is realized because the numerical integration of the differentiated fundamental solutions needs to be performed only twice for two-dimensional problems and three times for three-dimensional problems. Finite differencing of the boundary contours or surfaces,  $\partial x_m / \partial V_i$ , would still be necessary if the design variables could not be expressed as closed-form functions of the boundary contour or surface.

In this research, implicit differentiation of the fundamental solution has been avoided for a slightly more expensive method of finite differencing the coefficient matrices  $[d\mathbf{C}/d\mathbf{V}]$ ,  $[d\mathbf{H}/d\mathbf{V}]$  and  $[d\mathbf{G}/d\mathbf{V}]$ . For example,

$$\left[ \frac{\partial \mathbf{H}}{\partial V_i} \right] = \frac{[\mathbf{H}(V_i + \Delta V_i)] - [\mathbf{H}(V_i)]}{\Delta V_i} \quad (49)$$

The boundary needs to be integrated once for every design variable perturbation. Its only advantage over implicit differentiation was that it was very easy to program, particularly because it did not require the implementation of hyper-singular integration. Since most CPU time is involved in the factorization of the coefficient matrix  $[\mathbf{A}]$ , rather than during the integration over the boundary, this method still provided a substantial reduction in computational time at the expense of the memory required to store two sets of BEM coefficient matrices (Martin et al. [20]).

Implicit differentiation of the objective and constraint functions yields substantial savings because of the ability to re-use the previous inversion of the BEM coefficient matrix,  $[\mathbf{A}]^{-1}$ . The linear system of equations can then be solved for the unknown derivatives of temperature and flux  $\partial T / \partial V_i$  and  $\partial q / \partial V_i$ . The inversion of the coefficient matrix  $[\mathbf{A}]$  has not changed from the heat conduction analysis of the original design.

$$[A]^{-1} \left\{ \frac{\partial X}{\partial V_i} \right\} = -[C']\{T\} - [H']\{T\} + [G']\{Q\} + \left\{ \frac{\partial F}{\partial V_i} \right\} \quad (50)$$

#### 4.1.1 Gradients of the thermal objective functions

The gradient of each of the three thermal objective functions has been computed given the thermal sensitivity coefficients of  $\partial T / \partial V_i$  and  $\partial q / \partial V_i$ . These quantities are then used in the differentiated objective function. The gradient of the integrated temperature objective appears as follows, including the differentiation of the boundary Jacobian,  $|\bar{\eta}|$ , with respect to the design variable vector,  $V_i$ .

$$\frac{\partial F(V_i)}{\partial V} = \int_{\Gamma} 2(T - \bar{T}) \left( \frac{\partial T}{\partial V_i} - \frac{\partial \bar{T}}{\partial V_i} \right) d\Gamma + \int_{\Gamma} (T - \bar{T})^2 \frac{\partial |\bar{\eta}|}{\partial V_i} d\xi \quad (51)$$

When the mean temperature is used rather than a constant target temperature, the implicitly differentiated mean temperature has its own sensitivity.

$$\frac{\partial \bar{T}}{\partial V_i} = \frac{\int_{\Gamma} \frac{\partial T}{\partial V_i} d\Gamma + \int_{\Gamma} T \frac{\partial |\bar{\eta}|}{\partial V_i} d\xi}{\int_{\Gamma} d\Gamma} - \bar{T} \frac{\int_{\Gamma} \frac{\partial |\bar{\eta}|}{\partial V_i} d\xi}{\int_{\Gamma} d\Gamma} \quad (52)$$

The gradient of the net heat flux objective has also been derived for temperature-dependent thermal conductivity. The implicit differentiation requires the use of BEM design sensitivities of the flux as well as of the temperature when the thermal conductivity is temperature-dependent.

$$\frac{\partial F(V_i)}{\partial V_i} = - \int_{\Gamma_O} \frac{\partial Q}{\partial V_i} d\Gamma = \int_{\Gamma_O} k \frac{\partial (\partial T / \partial n)}{\partial V_i} d\Gamma + \int_{\Gamma_O} \frac{dk}{dT} \frac{\partial T}{\partial V_i} \frac{\partial T}{\partial n} d\Gamma + \int_{\Gamma_O} k \frac{\partial T}{\partial n} \frac{\partial |\bar{\eta}|}{\partial V_i} d\xi \quad (53)$$

#### 4.1.2 Gradients of the thermal constraint functions

Greater potential savings of computational resources can be achieved with the use of implicit differentiation for the computation of gradients of the constraint functions. For a thermally constrained shape optimization problem, the temperature field needs to be computed in order to determine the maximum temperature. Therefore, a BEM solution of the non-linear heat conduction equation is required for every constraint function analysis just as it was for the thermal objective function analysis. When the constraints are active or violated, the gradient of the constraint function with respect to the design variables is needed in order to project the searching directions. These gradient calculations are often needed for the gradient-based constraint restoration procedure that restores infeasible designs back to feasible regions. The implicitly differentiated inequality and equality constraint functions have the following form:

#### 4.2 I

A no  
consi  
Impl  
accur  
discr  
force

Since  
the c  
temp  
multi  
TI  
sensit  
 $\bar{U}$  as  
matrix  
factor  
comp  
true  
factor  
due to  
At  
the ne

#### 4.3 E

A two  
for de  
proble  
chose  
shape  
intern  
condu  
therm  
the in  
functi



$$\frac{\partial h(V_i)}{\partial V_i} = \frac{1}{T_{\max}} \left. \frac{\partial T}{\partial V_i} \right|_{\text{at } T_{\max}} \quad (54)$$

#### 4.2 Implicit differentiation for thermo-elastic design sensitivities

A new formulation for structural design sensitivity was developed for elastic solids to consistently account for the effects of thermal expansion along with centrifugal loading. Implicit differentiation of the governing system was shown to be capable of generating accurate sensitivities without the need for domain integration (Kane & Saigal, [50]). The discretized form of the boundary integral equation for thermo-elasticity with centrifugal body forces was differentiated with respect to the set of design variables,  $V_i$ .

$$\begin{aligned} [\partial \mathbf{H} / \partial V] \{ \mathbf{U} \} + [\mathbf{H}] \{ \partial \mathbf{U} / \partial V \} &= [\partial \mathbf{G} / \partial V] \{ \mathbf{P} \} + [\mathbf{G}] \{ \partial \mathbf{P} / \partial V \} + [\partial \mathbf{D}_n / \partial V] \{ \Psi \} \\ &+ \frac{1-2\nu}{2(1-\nu)} \left\{ \left[ \partial \mathbf{G}_g / \partial V \right] \left\{ \frac{\partial \Psi}{\partial n} - \gamma \mathbf{Q} \right\} - \left[ \mathbf{G}_g \right] \{ \gamma \partial \mathbf{Q} / \partial V \} - \right. \\ &\left. \left[ \partial \mathbf{H}_h / \partial V \right] \{ \Psi - \gamma (T - T_0) \} + [\mathbf{H}_h] \{ \gamma \partial T / \partial V \} - [\partial \mathbf{E}_n / \partial V] \Psi_0 \right\} \end{aligned} \quad (55)$$

Since the centrifugal body force field is not a function of the design variables, the sensitivity of the centrifugal potential function is neglected,  $\partial \Psi / \partial V = 0$ . The design sensitivities of the temperature,  $T$ , and flux,  $Q$ , do affect this equation. The formulation is compatible with multiple boundary element zones.

This sensitivity equation can be solved for the unknown displacement and traction sensitivities on the boundary given the boundary conditions  $\partial \bar{\mathbf{U}} / \partial V = 0$  and  $\partial \bar{\mathbf{P}} / \partial V = 0$  where  $\bar{\mathbf{U}}$  and  $\bar{\mathbf{P}}$  were specified on the direct problem. The advantage is that the BEM coefficient matrix factorization can be saved and reused in the design sensitivity analysis. This factorization process (using either a standard LU decomposition or SVD) is generally the most computationally demanding part of the overall boundary element analysis. This is especially true for three-dimensional turbine blades because of the very large dense matrices to be factored and because the SVD solver is usually needed because the matrix is ill-conditioned due to the thin turbine blade walls and coating.

Another source of savings is that the boundary stress sensitivities can be obtained without the need for additional integration or matrix factorization.

#### 4.3 Example of constrained thermal optimization using implicit design sensitivities

A two-dimensional example of the potential practical benefits of using implicit differentiation for design sensitivity analysis has been demonstrated on a thermally constrained optimization problem for internally cooled configurations. A Rankine oval external shape (Figure 6) was chosen to simulate a typical support strut airfoil while its symmetry throughout the geometric shape optimization procedure would demonstrate the accuracy and validity of the method. The internally cooled strut airfoil was modeled as being made of stainless steel with thermal conductivity  $k = 30.0$  W/m K and having a 150 micron-thick thermal barrier coating with thermal conductivity  $k = 1.0$  W/m K. Twenty geometric design variables were used to develop the internally-cooled strut airfoil design: 8 beta-spline vertices for the airfoil wall thickness function, 2 x-locations for end-points of each strut, 1 thickness for each strut, and 1 super-

elliptic exponent for the filleting of each strut. The coolant mass flow rate,  $\dot{m}$ , external hot gas temperature,  $T_{inlet}$ , and the coolant wall roughness,  $\epsilon_n$ , were also included into the design variable set. It was assumed to have four coolant flow passages that were initially symmetrically sized and located (dotted lines in Figure 6). Coolant heat transfer coefficients,  $h_{cool,n}$ , and bulk temperatures,  $T_{cool,n}$ , were applied as boundary conditions to the four internal coolant walls.

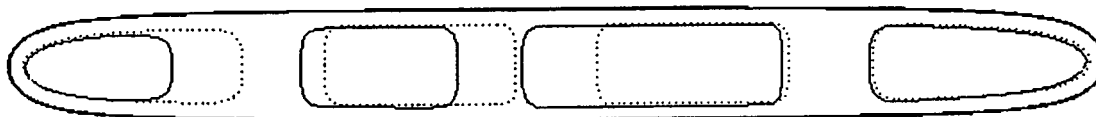


Figure 6: Rankine oval shape as an example of a symmetric airfoil. The initial guess (dotted lines) and final optimized (solid lines) shapes of the coolant passages are shown.

The conjugate aero-thermal analysis started with an initial guess as to the temperature on the outer wall of the Rankine airfoil. A Reynolds-averaged Navier-Stokes flow solver (Chima [35]) was used to predict the hot gas flow-field and the corresponding heat flux variation on the airfoil external surface. The Baldwin-Lomax turbulence model was used to approximate the turbulent boundary layer. Given a fixed hot gas ambient temperature,  $T_{inlet}$ , the iterative conjugate process was used to obtain a heat convection coefficient distribution on the external surface by iterating between the temperature and the heat flux boundary conditions on the outer surface of the airfoil. That heat transfer coefficient distribution (Figure 7) remained fixed during the optimization process. The target average temperature in the airfoil material was specified to be  $\bar{T} = 1300K$ . This optimization problem was constrained to have a maximum temperature of 1375 K.

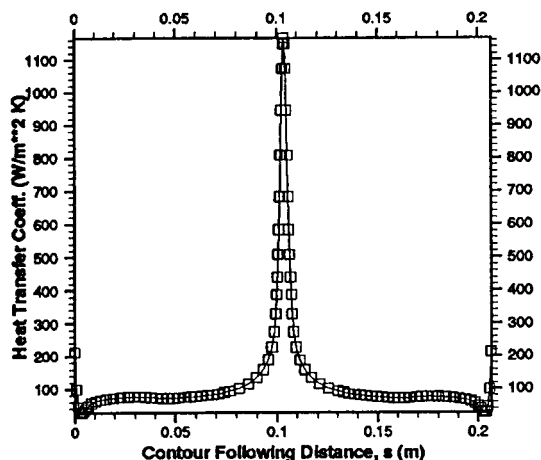


Figure 7: Heat transfer coefficient computed on outer surface of Rankine airfoil using the conjugate heat transfer prediction.

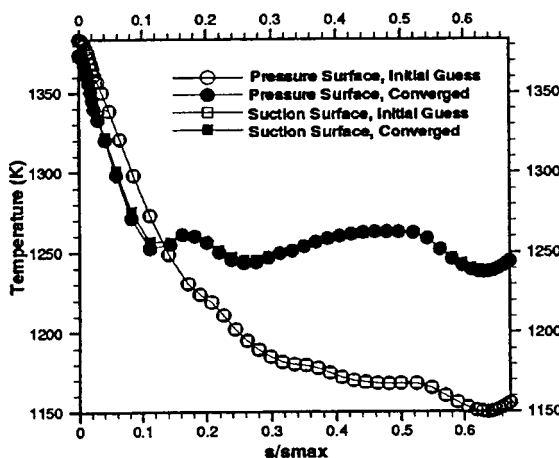


Figure 8: Temperatures computed by the BEM on outer surface of the Rankine oval corresponding to initial guess and optimized configurations.

Using conjugate and corresponding distributions, the temperature distribution is slightly significant. (Figure that the (Figure surface increase passage implicit the object improve different amount the imp obtained greater three-dimensional savings

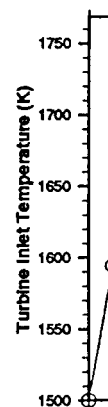


Figure 9

Using the flexible geometry treatment of the interior of the airfoil, and using the constrained conjugate heat transfer optimization procedure, the four coolant flow passages were modified and converged to their new shapes and locations (solid lines in Figure 6). The temperature distribution on the converged outer airfoil surface was more uniform than the initial surface temperature distribution. Even the leading edge stagnation point temperature had decreased slightly (Figure 8). At the same time, the optimized coolant passages allowed for a significantly higher inlet hot gas temperature (Figure 9) and a lower coolant mass flow rate (Figure 10). This is a remarkable result, although it is only a computational simulation. Notice that the final optimized geometry was symmetric about the x-axis. The coolant pressure loss (Figure 11) in the coolant passages increased because of the need for the increased relative surface roughness (Figure 12) on the walls of the coolant passages. This, in turn, led to the increased average convection heat transfer coefficients (Figure 13) on the walls of the coolant passages. The thermally constrained conjugate optimization was executed with and without implicit thermal design sensitivity. In the latter case, forward finite differencing was used for the objective function gradient evaluation. Implicit differentiation produced a significant improvement in both faster convergence and a lower minimum than did the explicit finite differencing (Figure 14). This figure shows that there is a substantial improvement in the amount of computing time required. Each symbol indicates an optimization cycle. Notice that the implicit solution required less than half the number of cycles. This improvement was obtained in a simple two-dimensional example that required only 17 optimization cycles. Even greater savings are expected for more complex problems. Since the coefficient matrices of three-dimensional geometries are larger than for two-dimensional problems, the potential savings are expected to be substantially greater for three-dimensional problems.

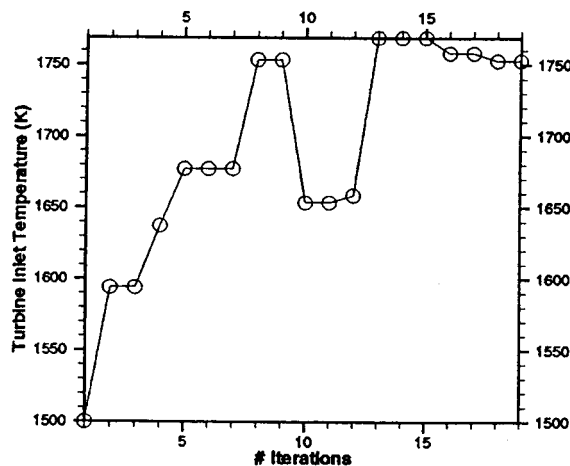


Figure 9: History of hot gas inlet temperature during constrained conjugate optimization of an internally-cooled symmetric airfoil.

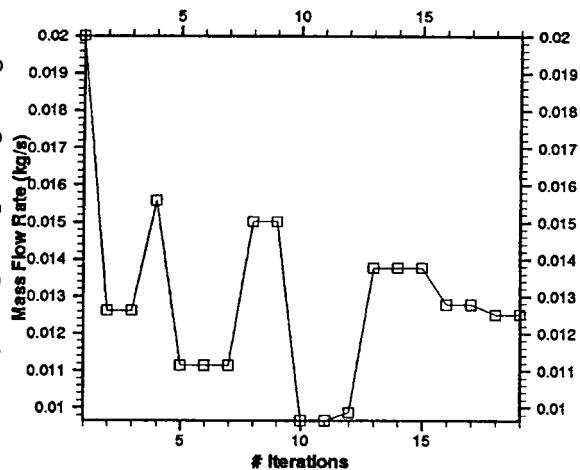


Figure 10: History of coolant mass flow rate during constrained conjugate optimization of an internally-cooled symmetric airfoil.

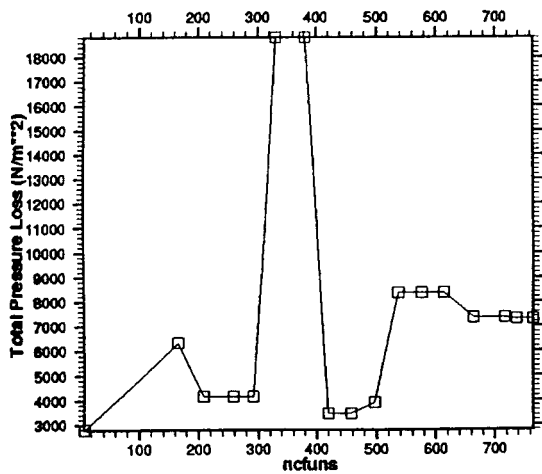


Figure 11: History of pressure loss in coolant passages during constrained conjugate optimization of an internally-cooled airfoil.

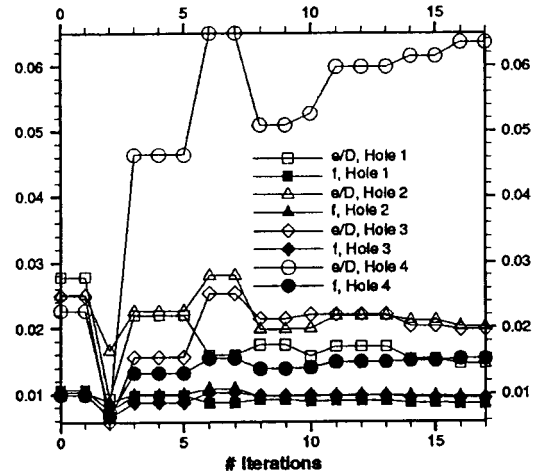


Figure 12: History of surface roughness during constrained conjugate optimization of an internally-cooled symmetric airfoil.

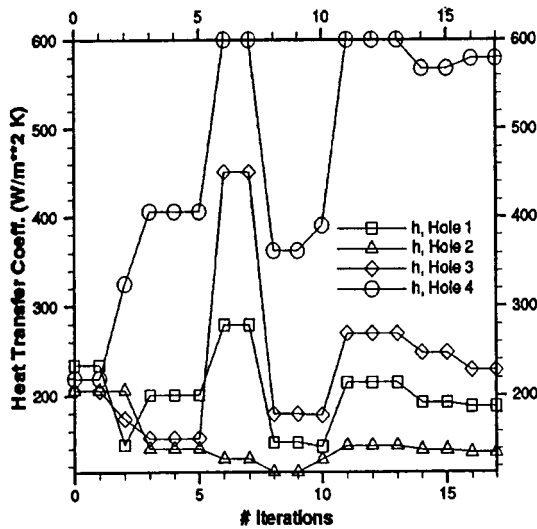


Figure 13: History of coolant heat transfer coefficients during constrained conjugate optimization of an internally-cooled airfoil.

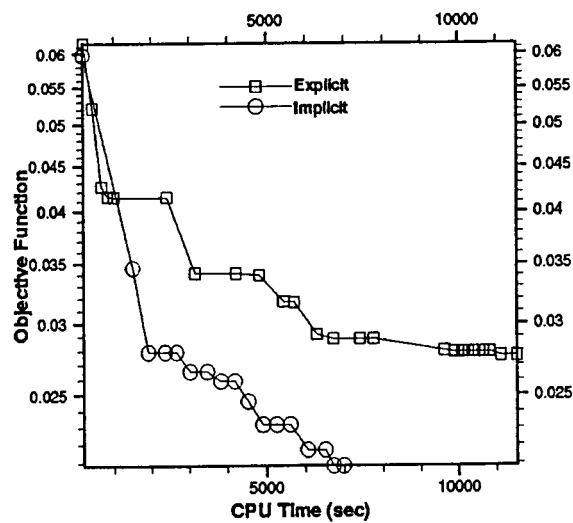


Figure 14: Convergence history of target temperature objective function during constrained conjugate optimization of an internally-cooled airfoil.

Es  
solve  
probl  
elastic  
30:1.

#### 4.4 C

In or  
with  
impli  
design  
range  
errors  
errors  
step s

Gr  
tempe  
oval o  
finite  
found  
previo  
lists t  
( $V_{min}$   
Notic  
range  
domin  
Ge  
or the  
functi  
step s  
with  
deriva  
thickr

Table

Des
$\beta$ -S
Str
Str
Wa
Coc
Tur

Estimates have shown that two-dimensional constrained optimization problems can be solved in one quarter of the computing time, while three-dimensional thermally constrained problems have a 20:1 advantage in the computing time. Preliminary estimates of the thermo-elastically constrained problem have indicated the savings in the computing time to be about 30:1.

#### 4.4 Comparison of finite differencing to implicit differentiation

In order to improve performance, sensitivity gradients of the objective and constraint functions with respect to the geometric and boundary condition design variables were obtained using implicit differentiation of the boundary element system of equations. The accuracy of the design sensitivity was studied with respect to forward and central finite differences over a range of differencing step sizes. We have found that there is a trade-off between truncation errors and round-off errors that is dependent upon the type of design variable. Truncation errors are larger with bigger differencing step sizes, but round-off errors are larger with smaller step sizes.

Gradients of the uniform temperature objective function (eqn 57) and maximum temperature constraint function (eqn 60) were determined on the initial guess of the Rankine oval constrained conjugate optimization problem. The gradients were obtained over a range of finite differencing step sizes. These step sizes were given with respect to the base step sizes found in Table 1. These base step sizes were those that were manually chosen and used in the previous Rankine oval optimization example. The Rankine oval chord was 0.2 m. Table 1 also lists the design variable bounds,  $V_{\min}$  and  $V_{\max}$ , and the gradient is non-dimensionalized by  $(V_{\min} - V_{\max})$ . The trade-off between truncation and round-off error is apparent in Figure 15. Notice that the derivative of the uniform temperature objective function is accurate over a wide range of differencing step sizes. As the step size becomes bigger, the truncation error dominates. The implicit derivative is as accurate as the central differenced derivative.

Geometry parametric variables have larger round-off errors than do the beta-spline vertices or the boundary condition variables (Figure 16). The derivative of the thermal objective function with respect to the strut centerline coordinate has round-off errors that are dominant in step sizes below  $10^{-1}$  of the base perturbation. The central differenced derivative coincides with the implicit derivative between  $10^{-1}$  and  $10^1$ , while the forward explicit differenced derivative is invalid below the base step size. Similar behavior was apparent for the strut thickness variable shown in Figure 17.

Table 1: Perturbation step sizes used for comparing design sensitivities using explicit finite differencing and implicit differentiation for the symmetric airfoil case.

<i>Design Variable</i>	<i>Base Step Size</i>	<i>Design Variable Range</i>
$\beta$ -Spline Vertex	0.001*chord	0.1 – 5.0 mm
Strut Centerline Coordinate	0.001*chord	Dependent (+/- 5 mm)
Strut Thickness	0.001*chord	Dependent (0 – 5 mm)
Wall Roughness	0.001 mm	0.0 – 0.05
Coolant Mass Flow Rate	0.0001 kg/s	0.005 – 0.05 kg/s
Turbine Inlet Temperature	1 K	1000 – 2000 K

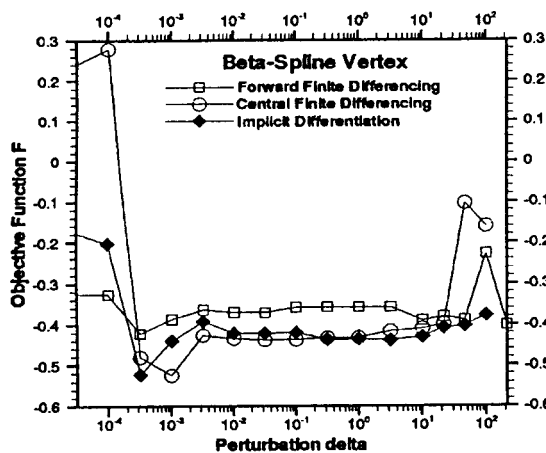


Figure 15: Finite differenced versus implicitly differentiated target temperature objective function with respect to beta spline vertices.

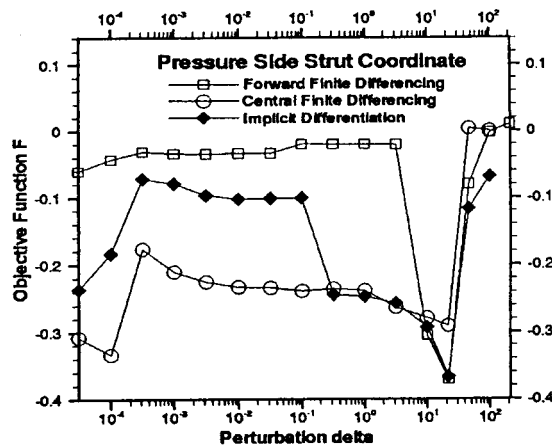


Figure 16: Finite differenced versus implicitly differentiated target temperature function with respect to strut coordinates.

The boundary condition design variables were less sensitive to round-off errors than the geometry parameters, but the implicit derivatives tended to have a slight bias caused by the non-linearity of the boundary condition. The examples of these types of derivatives with respect to the wall roughness, coolant mass flow rate and turbine inlet temperature design variables are demonstrated in Figures 18, 19 and 20, respectively.

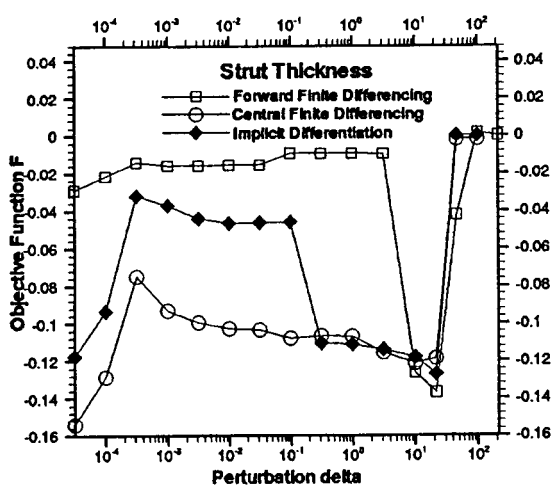


Figure 17: Finite differenced versus implicitly differentiated uniform temperature objective function with respect to strut thickness.

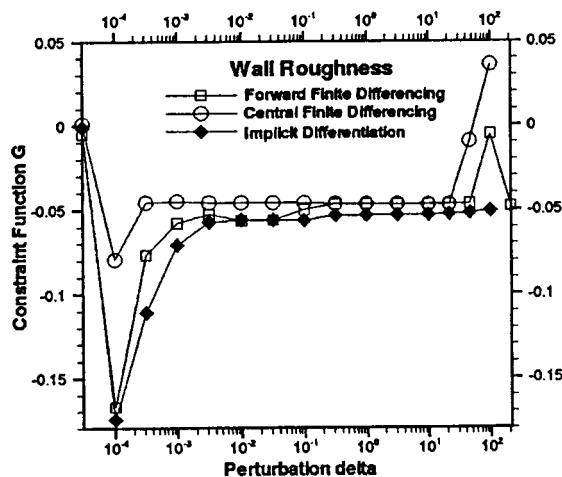


Figure 18: Finite differenced versus implicitly differentiated maximum temperature with respect to coolant passage wall roughness.

0.25  
0.2  
0.15  
0.1  
0.05  
0  
-0.05  
-0.1  
-0.15  
-0.2

Figure

TL  
tempe  
functi  
the he  
flux d  
solver  
coolan  
could

5 Tu

This  
intern  
althou  
These  
analys  
object  
been 1

5.1 T

The b  
linear  
object  
with t

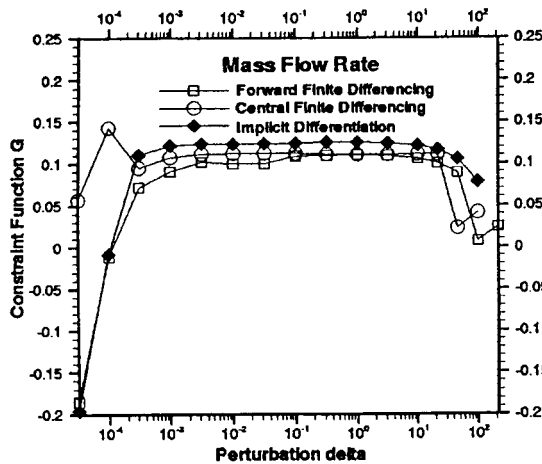


Figure 19: Finite differenced versus implicitly differentiated maximum temperature constraint with respect to coolant flow rate.

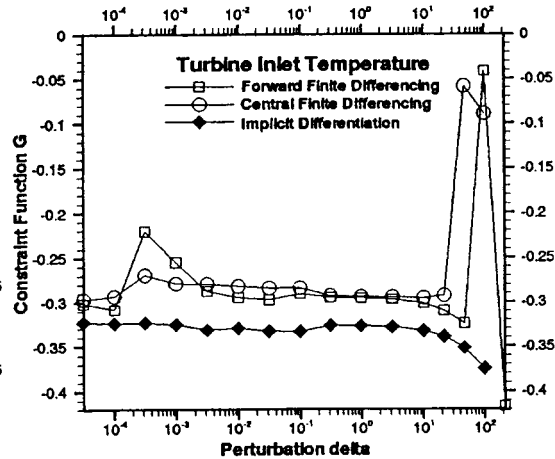


Figure 20: Finite differenced versus implicitly differentiated maximum temperature constraint with respect to turbine inlet temperature.

The implicit BEM system was linearized and solved non-iteratively for the derivatives of temperature and heat flux, but the bulk coolant temperatures were actually a non-linear function of the heat flux. The bias is especially evident in the turbine inlet temperature because the heat flux is a strong function of that variable. The implicit system was solved for the heat flux derivatives using a guess as to the heat flux in the quasi-one-dimensional coolant network solver. That guessed heat flux was taken from the conjugate solution of the unperturbed coolant configuration. Incorporating the heat flux non-linearity in the implicit BEM system could probably alleviate the bias.

## 5 Turbine cooling scheme optimization

This section will present a few example cases of thermally constrained optimization of internally cooled turbine blades. Only two-dimensional examples will be discussed here, although both two- and three-dimensional optimization programs were developed and tested. These optimizations have incorporated the fully coupled aero-thermal conjugate heat transfer analysis, but no thermo-elastic constraint was incorporated into them. Results with thermal objective functions will be shown, but the aero-thermal or engine cycle objectives have not yet been fully explored.

### 5.1 Turbine cooling scheme optimization for uniform temperature

The behavior of the uniform temperature objective was studied first on a generic axial turbine linear airfoil cascade. The optimization objective function was the uniform temperature objective (eqn 1) using a target temperature,  $\bar{T}$ . The thermal optimization was constrained with the maximum temperature equality constraint function (eqn 3). All cases discussed in this

section used the conjugate thermal analysis and the fully-coupled quasi-one-dimensional model for the coolant flow passages.

In the conjugate procedure for the aero-thermal analysis of the objective, the optimization program was started with a CFD analysis of the turbine cascade (Arts et al. [53]) using an unstructured compressible turbulent Navier-Stokes solver (Han & Liu [34]) and an initial guess for the temperature,  $T_O$ , on the turbine blade surface. The CFD solver used the turbine inlet total temperature,  $T_{t,inlet}$ , inlet total pressure,  $p_{t,inlet}$ , exit static pressure,  $p_{exit}$ , and inlet Mach number,  $M_{inlet}$ , for its boundary conditions (see Table 2). Once converged, the flow-field analysis code computed turbulent heat fluxes,  $Q_O$ , that were applied as boundary conditions directly to the non-linear BEM heat conduction analysis code. After converging on the non-linear boundary conditions of the coolant passages, new blade surface hot wall temperatures were computed by the BEM. Since this wall temperature variation was, in general, different from the wall temperatures specified to the hot gas flow-field analysis code, they were applied again as boundary conditions to the CFD code. A new CFD solution then returned heat fluxes that were again different from those used initially. This process was repeated several times until finally the heat fluxes converged in about 9-12 global coupling iterations. Thereafter, heat transfer coefficients on the outer airfoil boundary were computed from the converged hot surface temperatures and fluxes and the corresponding total turbine inlet temperature,  $h_O = Q_O / (T_O - T_{Oinlet})$ . The heat transfer coefficient variation then remained fixed for a number of optimization cycles set by the user. This global conjugate computation was performed after every ten optimization cycles. Figure 21 illustrates the different variations of blade hot surface heat fluxes computed after subsequent iterations of the semi-conjugate procedure. In this figure, each intermediate flux ( $dT/dn$ ) variation is shown in dotted lines and the solid line shows the optimized flux. The computed heat transfer coefficient distribution on the outer turbine airfoil is shown in Figure 22. The constrained hybrid numerical optimization used the geometric and cooling scheme design variables listed in Table 3. The coolant wall roughness, coolant mass flow rate and turbine inlet temperature were all design variables.

Table 2: List of boundary conditions and constants for the uniform temperature optimization of a turbine blade.

<i>Boundary Conditions</i>	<i>Value</i>
$p_{inlet}$	588,131 Pa
$p_{exit}$	134,115 Pa
Inlet Mach number	0.1772
$T_{inlet}$ (initial guess)	1592.6
$k_l$	1.0 W/m K
$k_M$	30.0 W/m K
C	0.1 mm

Table 3: Design variables used for uniform temperature thermal optimization of an internally cooled turbine blade.

<i>Design Variable</i>	<i>#</i>
Beta-Spline Wall Thickness	8
Strut Coordinates (2 per strut)	6
Strut Thickness (1 per strut)	3
Strut Filleting (2 per strut)	6
Wall Roughness (1 per passage)	4
Mass Flow Rate	1
Turbine Inlet Temperature	1

1E+07  
9E+06  
8E+06  
7E+06  
6E+06  
5E+06  
4E+06  
3E+06  
2E+06  
1E+06  
0

Fig

Figure



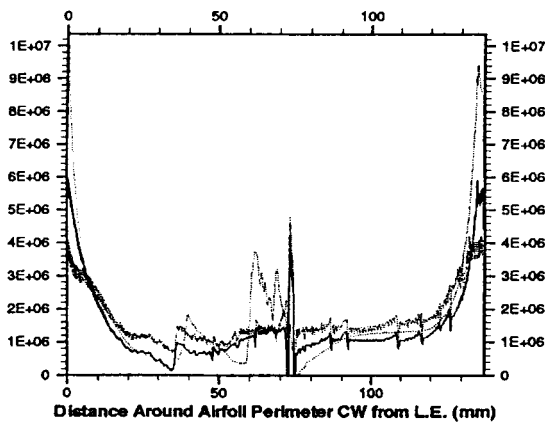


Figure 21: Fluxes ( $dT/dn$  in K/m) computed by the CFD on the surface of the turbine blade for the conjugate coupling procedure.

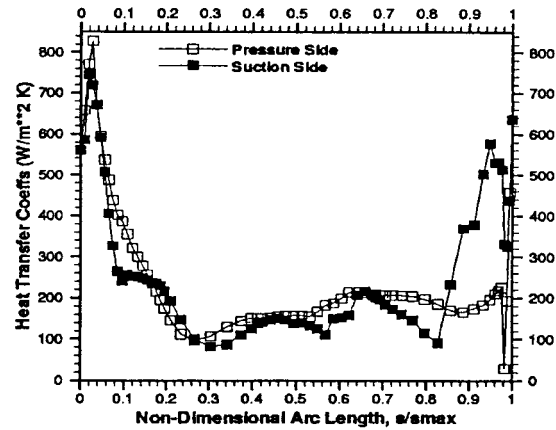


Figure 22: Heat transfer coefficient predicted by CFD on the outer turbine airfoil boundary.

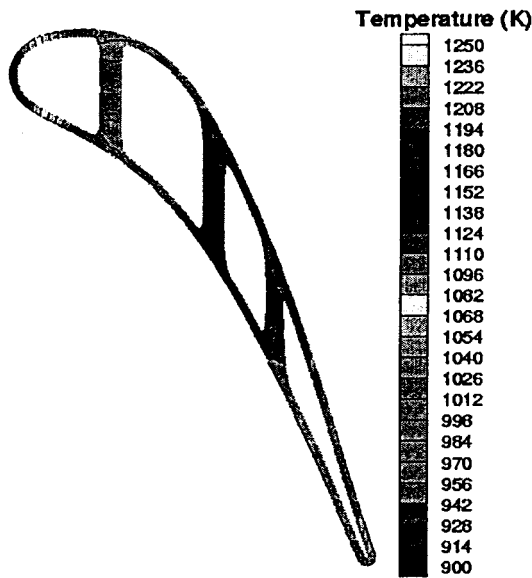


Figure 23: Temperature field computed by the BEM for the initial guess of the boundary conditions on internally cooled and thermal barrier coated turbine blade.

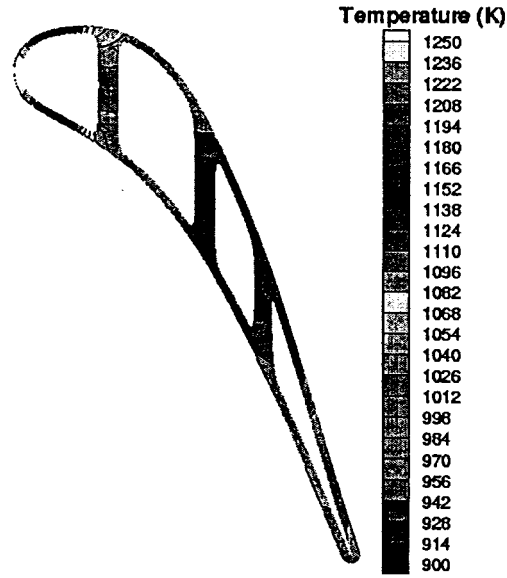


Figure 24: Temperature field computed by the BEM for the first feasible set of boundary conditions on an internally cooled and thermal barrier coated blade.

The total number of design variables was 29. A target temperature of the uniform temperature objective was 1100 K. The maximum temperature equality constraint was enforced during the entire optimization process. Implicit design sensitivity was used to compute the gradients of the objective and constraint functions. The thermal optimization algorithm was started with the initial guess shown along with flooded temperature contours computed by the BEM in Figure 23. In this example, the thickness of the thermal barrier coating was kept fixed. The initially guessed wall roughness ratio on each hole was  $\epsilon/Dh = 0.05$ , the initially guessed coolant mass flow rate was 0.025 kg/s, and the initially guessed total turbine inlet temperature was 1600 K. The genetic algorithm population size was held at 16 members, and the percentage chance of mutation in the genetic algorithm was specified to be 3% per breeding pair. The crossover process of the genetic algorithm used a random linear interpolation between two population members selected by a roulette wheel.

The first numerical heat conduction analysis of the initial guess (Figure 23) predicted a maximum temperature of around 1160 K. The first thing that the constrained hybrid optimization program did was to restore the design to one that had a maximum temperature of 1250 K. That is, the geometry was fixed while the coolant wall boundary conditions were modified using a gradient-based (DFP) minimization of the equality constraint function until it was feasible. This required two sub-optimization cycles to restore the initial design to feasibility, and the corresponding temperature contours are shown in Figure 24.

The constrained hybrid optimizer did this many times during the course of the entire procedure (at least once for every infeasible design produced by the DFP, GA, NM or SA), and each sub-optimization of an infeasible design required about 1-3 sub-cycles to restore the constraint. These constraint minimizations utilized implicit differentiation to obtain the quasi-second-order gradient, and each implicit gradient evaluation needed less than one tenth of the CPU time than a normal heat conduction analysis.

The typical constrained hybrid numerical optimization algorithm ran for less than 8 hours on a single vector processor Cray C-90, and required 997 computational heat conduction analyses, 37 optimization cycles and 5 conjugate CFD analyses in order to reach a converged solution. The optimization was started with the GA and ran for 12 iterations before switching automatically to the NM optimizer. The hybrid optimizer then switched back and forth to the SA algorithm when the NM failed after 3 iterations. The remainder of the optimization cycles (about 20 iterations) utilized all four algorithms (DFP, GA, NM and SA) until the program ended when all four algorithms failed to improve the objective function. The most significant modifications to the design occurred during the first 8 optimization cycles and the program only slightly modified the designs in the remaining cycles. The final optimized configuration with temperature contours is shown in Figure 25.

The optimization process produced a very uniform temperature field in the blade (Figure 25 & 26). It became apparent that the program was trying to make the bulk coolant temperatures equal to the maximum temperature,  $\overline{T}_{\max}$ , while increasing the internal heat transfer coefficients to infinity. This example reached a global minimum where the mean temperature and bulk coolant temperatures were as close as possible to the maximum temperature in the metal (Figures 26 & 27). The optimization algorithm accomplished this by increasing the coolant heat transfer coefficients (mainly wall roughness) up to their limiting values of 2400.0 W/m<sup>2</sup> K (Figure 28). The coolant mass flow rate remained relatively the same (Figure 29) while the turbine inlet temperature increased dramatically (Figure 30).



Figur



Figur

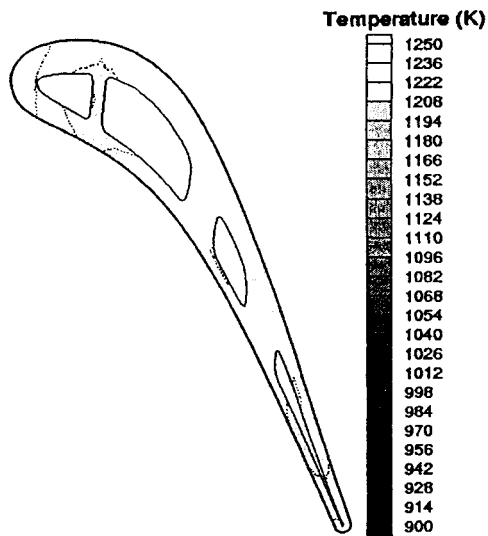


Figure 25: Temperature field computed on optimized internally cooled turbine blade using uniform target temperature objective.

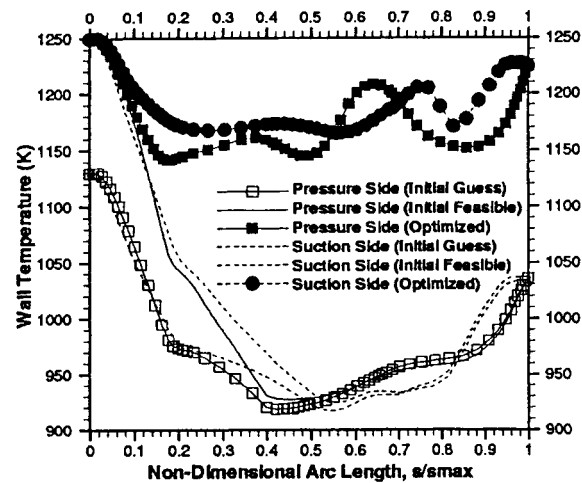


Figure 26: Wall temperature variation on optimized turbine blade using uniform target temperature objective.

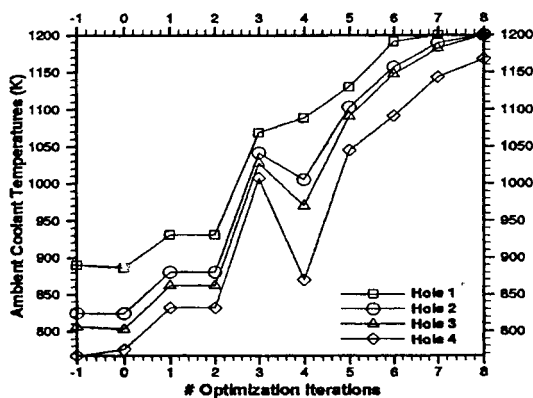


Figure 27: Evolution of bulk coolant temperatures during thermal optimization for uniform mean temperature objective.

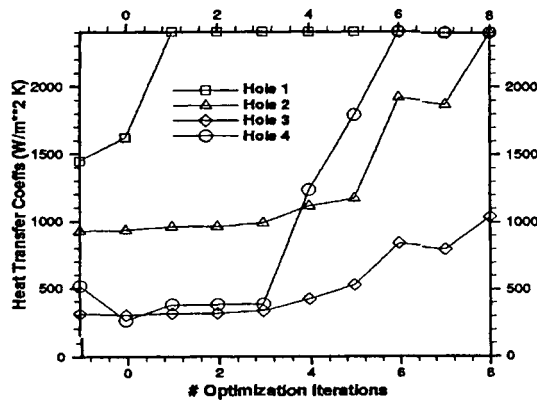


Figure 28: Evolution of heat transfer coefficients on coolant walls during thermal optimization for uniform mean temperature objective.

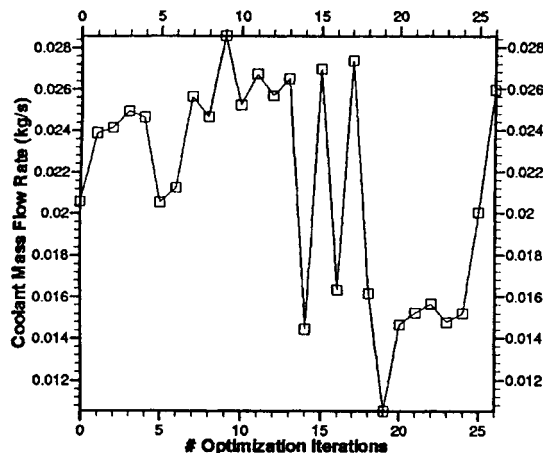


Figure 29: History of coolant mass flow rate for uniform mean temperature objective in the blade material.

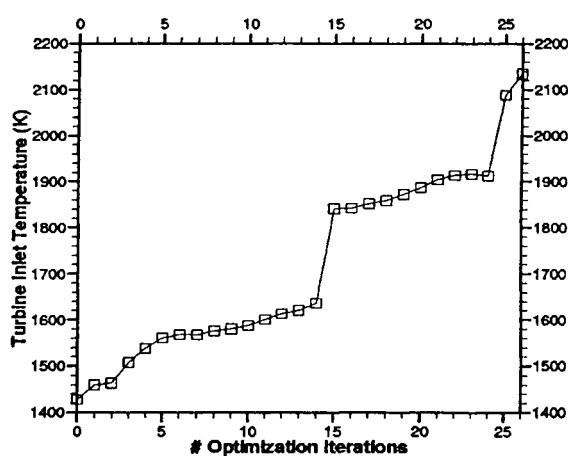


Figure 30: History of turbine inlet hot gas temperature for uniform mean temperature objective in the blade material.

## 5.2 Turbine cooling scheme optimization for maximum heat flux

Although the uniform temperature objective did have some desirable features, it has been concluded that it does not satisfy the criterion established for internal coolant passage optimization. Some of the optimization runs for a uniform target temperature were successful in increasing the turbine inlet temperature while decreasing the mass flow rate, but this behavior was not consistent. In an effort to try to maximize the turbine inlet temperature only, the net heat flux absorbed by the coolant was explicitly maximized. Obviously, an increase in turbine inlet temperature would lead directly to an increase in heat flux. This was expected because an increase in the convection heating on the outer surface of the turbine blade would require more cooling to sustain the heat loads.

The thermal optimization problem for maximum integrated heat flux (eqn 4) began with an initial guess identical to the one presented in the previous section except for the change in the objective. Thermal integrity was maintained with the enforcement of the equality constraint on the maximum temperature. The quasi-conjugate procedure for coupled aero-thermal heat transfer was used every ten optimization cycles. Implicit thermal design sensitivity was used to compute the gradients of the heat flux objective and the maximum temperature equality constraint. This optimization did well to increase the turbine inlet temperature. In fact, it always reached its turbine inlet temperature bound and the program remained relatively fixed on that design variable boundary for the remaining cycles. The boundary conditions variables (wall roughness, mass flow rate and turbine inlet temperature) were more influential than the geometric variables. The optimized bulk temperatures of the coolant air were higher (Figure 31) indicating the increased amount of heat absorbed by the coolant air with increasing heat flux. There were large increases in the heat flux at the leading and trailing edges (Figure 32). This optimized design nearly doubled the pressure losses in the coolant passages resulting from very high values of the optimized surface roughness.

Th  
was c  
increa  
on ho  
conve  
that th  
at 240  
conve  
time i  
Th  
netwo  
be acc  
K. A  
tempe  
integi

Figure

The coolant mass flow rate remained relatively the same because the coolant inlet pressure was coupled to the bulk coolant temperature. The increased internal wall friction (Figure 33) increased the internal heat transfer coefficients (Figure 35). High heat transfer was not needed on hole two and three so their wall roughness stayed relatively the same. Figure 34 shows the convergence history of the turbine inlet temperature during the maximization process. Notice that the temperature was increased from an initial guess at 1600 K to the design variable bound at 2400 K, and it remained fixed there until the optimization process became stationary. The convergence history of the integrated heat flux (objective function) is shown versus computing time in Figure 36.

This dramatic improvement indicates that it is possible to design an internal turbine coolant network for extremely high temperatures using only internal cooling techniques, but it can only be accomplished if the heat transfer enhancements can provide coefficients up to  $2000 \text{ W/m}^2 \text{ K}$ . As mentioned before, this is only an academic exercise limited by only a maximum temperature constraint. Results from a real turbine under stricter thermal and structural integrity constraints will probably be less dramatic.

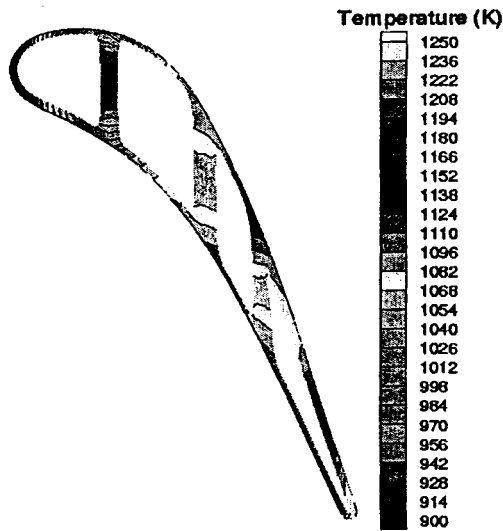


Figure 31: Temperature field in a turbine blade optimized for a maximum integrated surface heat flux.

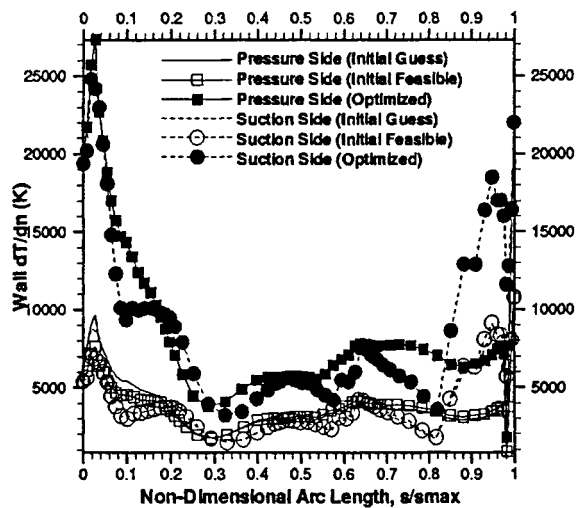


Figure 32: Variation of heat flux on outer surface of turbine blade optimized for a maximum integrated surface heat flux.

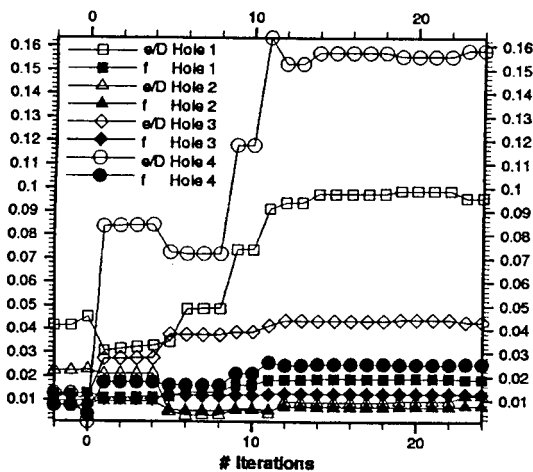


Figure 33: Evolution of coolant passagewall relative roughness and friction factor during heat flux maximization.

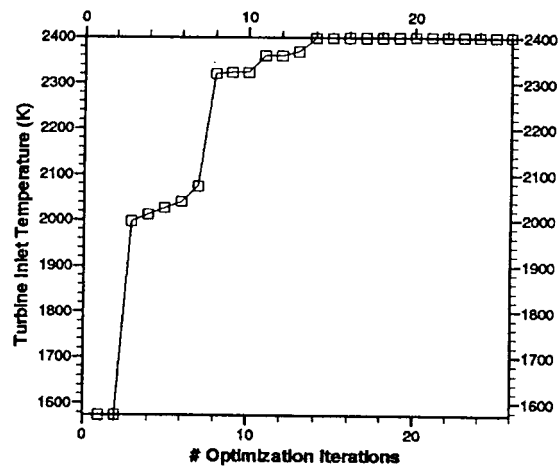


Figure 34: History of turbine inlet hot gas temperature design variable during heat flux maximization.

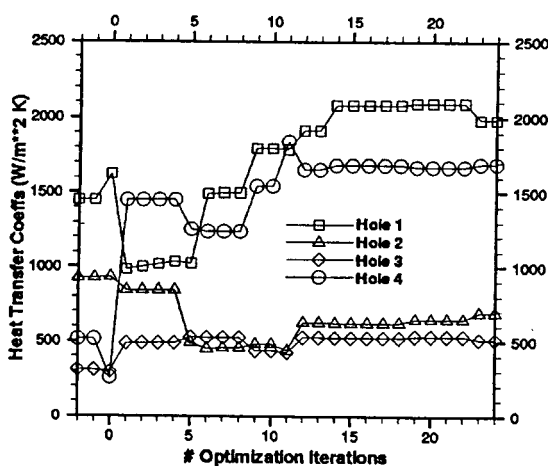


Figure 35: Evolution of heat transfer coefficients on walls of the four internal coolant passages during heat flux maximization.

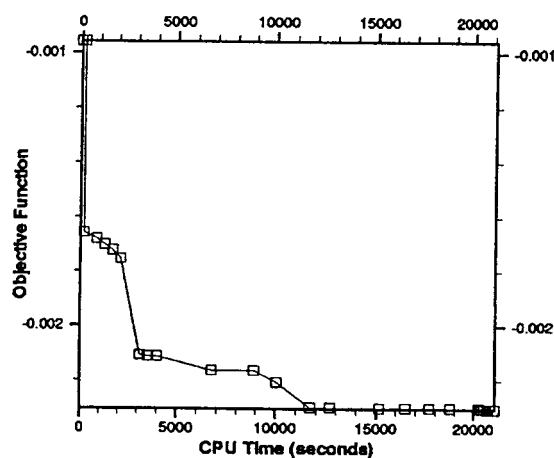


Figure 36: Convergence history of the integrated heat flux versus computing time during heat flux maximization.

### 5.3 Conclusions

A multi-disciplinary aero/thermal design and optimization methodology combines computational aerodynamics, thermodynamics and turbine cooling systems geometry generation software into a fully computer-automated design tool for the optimization of

inter  
coup  
obje  
redu  
to e  
simu  
incre  
effic  
simp  
exist  
T  
inter  
aero  
betw  
thrus  
analy  
struc  
of th  
provi  
impr

### Ack

The  
DMI-  
NAG  
Kestu  
Oatw.

### Refe

[1]

[2]

[3]

[4]

[5]

[6]

internally cooled turbine blades with thermal barrier coatings. These analysis tools were coupled with a hybrid optimization algorithm in order to minimize a thermal optimization objective function. The minimization of the uniform temperature function reflected the reduction in thermal stresses while the cooling scheme did not allow the maximum temperature to exceed the temperature limitations of the metal blade. The heat flux maximization with simultaneously enforced maximum temperature constraints allowed the optimization system to increase the turbine inlet temperature for an improvement in the turbomachinery engine efficiency. Significant increases in the turbine inlet gas temperature were realized on a simplified internally cooled turbine blade, although this algorithm has yet to be verified on an existing turbine blade design.

This multi-disciplinary research effort has already continued with the integration of the internally cooled engine cycle analysis to account for the coolant losses as well as the aerodynamic turbine efficiency. The use of this objective will quantify a proper trade-off between coolant flow rate and turbine inlet temperature in order to maximize engine specific thrust or thrust-specific fuel consumption. The temperature computed from the conjugate analyses was incorporated into the thermo-elastic response for a rigorous development of the structural constraint. Ultimately, the resulting thermal loads in the turbine blade and the effects of the thermo-elastic deformation on the flow field can be built into the design process, providing a turbine designer with a tool for confidently enlarging the current design space and improving the performance of the turbine cooling scheme.

## Acknowledgments

The authors would like to express their gratitude for the National Science Foundation Grant DMI-9522854 monitored by Dr George A. Hazelrigg, the NASA Lewis Research Center Grant NAG3-1995 facilitated by Dr John K. Lytle and Dr Herbert J. Gladden and monitored by Dr Kestutis Civinskas, and the Lockheed Martin Skunk Works grant monitored by Mr Thomas Oatway.

## References

- [1] Lakshminarayana, B., *Fluid Dynamics and Heat Transfer of Turbomachinery*, John Wiley & Sons Inc., New York, NY, 1996.
- [2] Hill, P.G. & Peterson, C.R., *Mechanics and Thermodynamics of Propulsion, 2nd Edition*, Addison-Wesley Publishing Co., Reading, MA, 1992.
- [3] Brown, A., Jubran, B.A. & Martin, B.W., Coolant Optimization of a Gas Turbine Engine, *Proceedings of the Institute of Mechanical Engineers*, Vol. 207, pp. 31-47, 1993.
- [4] Mochizuki, S., Takamura, J., Yamawaki, S. & Yang, W.J., Heat Transfer in Serpentine Flow Passages With Rotation, *ASME Journal of Turbomachinery*, Vol. 116, pp. 133-140, 1994.
- [5] Kawaike, K., Anzai, S. & Sasada, T., Integrated CAE System for Cooled Turbine Blade Design and Verification Tests of Analytical Codes, in *Heat Transfer in Turbomachinery*, (eds R.J. Goldstein, D.E. Metzger, and A.I. Leontiev), Begell House Inc., New York, NY, pp. 73-84, 1992.
- [6] Ikeguchi, T. & Kawaike, K., Effects of Closed-Circuit Gas Turbine Cooling Systems on Combined Cycle Performance, ASME paper 94-JPGC-GT-8, October 2-6, 1994.

- [7] Kennon, S.R. & Dulikravich, G.S., The Inverse Design of Internally Cooled Turbine Blades, *ASME Journal of Engineering for Gas Turbines and Power*, Vol. 107, pp. 123-126, January 1985. [21]
- [8] Chiang, T.L. & Dulikravich, G.S., Inverse Design of Composite Turbine Blade Circular Coolant Flow Passages, *ASME Journal of Turbomachinery*, Vol. 108, pp. 275-282, 1986. [22]
- [9] Dulikravich, G.S. & Kosovic, B., Minimization of the Number of Cooling Holes in Internally Cooled Turbine Blades, *International Journal of Turbo & Jet Engines*, Vol. 9, No. 4, pp. 277-283, 1992. [23]
- [10] Dulikravich, G.S. & Martin, T.J., Inverse Design of Super-Elliptic Cooling Passages in Coated Turbine Blade Airfoils, *AIAA Journal of Thermophysics and Heat Transfer*, Vol. 8, No. 2, pp. 288-294, 1994.
- [11] Dulikravich, G.S. & Martin, T.J., Geometrical Inverse Problems in Three-Dimensional Non-Linear Steady Heat Conduction, *Engineering Analysis with Boundary Elements*, Vol. 15, pp. 161-169, 1995. [24]
- [12] Dulikravich, G.S., Inverse Design and Active Control Concepts in Strong Unsteady Heat Conduction, *Applied Mechanics Reviews*, Vol. 41, No. 6, pp. 270-277, 1988. [25]
- [13] Martin, T.J. & Dulikravich, G.S., Finding Temperatures and Heat Fluxes on Inaccessible Surfaces in 3-D Coated Rocket Nozzles, *1995 JANNAF Non-Destructive Evaluation Propulsion Subcommittee Meeting*, Tampa, FL, Dec. 4-8, 1995, Chemical Propulsion Information Agency - CPIA Publication 637, pp. 119-129, December 1995. [26]
- [14] Bendiksen, O.O., Aeroelastic Problems in Turbomachines, *Flight-Vehicle Materials, Structures, and Dynamics, Vol. 5, Structural Dynamics and Aeroelasticity*, (eds A.K. Noor, and S.L. Venneri), ASME, New York, NY, 1993. [27]
- [15] Dulikravich, G.S. & Martin, T.J., Inverse Shape and Boundary Condition Problems and Optimization in Heat Conduction, *Advances in Numerical Heat Transfer - Volume I* (eds W.J. Minkowycz and E.M. Sparrow), Taylor and Francis, 1996, pp. 381-426. [28]
- [16] Martin, T.J. & Dulikravich, G.S., Aero-Thermal Analysis and Optimization of Internally Cooled Turbine Airfoils, *XIII International Symposium on Airbreathing Engines (XIII ISABE)*, (ed F.S. Billig), Chattanooga, TN, ISABE 97-7165, Volume 2, pp. 1232-1250, September 8-12, 1997. [29]
- [17] Dulikravich, G.S., Martin, T.J., Dennis, B.H., Lee, E.-S. & Han, Z.-X., Aero-Thermo-Structural Design Optimization of Cooled Turbine Blades, *AGARD - AVT Propulsion and Power Systems Symposium on Design Principles and Methods for Aircraft Gas Turbine Engines*, NATO-RTO-MP-8 AC/323(AVT)TP/9, Toulouse, France, May 11-15, 1998. [30]
- [18] Dulikravich, G.S., Martin, T.J. & Han, Z.-X., Aero-Thermal Optimization of Internally Cooled Turbine Blades, *Fourth ECCOMAS Computational Fluid Dynamics Conference*, (eds K. Papailiou, D. Tsahalis, J. Periaux and D. Knoerzer), Athens, Greece, September 7-11, 1998, Vol. 2, pp.158-161, John Wiley & Sons, NY, 1998. [31]
- [19] Dulikravich, G.S., Martin, T.J., Dennis, B.H. & Foster, N.F., Multidisciplinary Hybrid Constrained GA Optimization, *EUROGEN '99 - Evolutionary Algorithms in Engineering and Computer Science: Recent Advances and Industrial Applications*, (eds K. Miettinen, M. M. Makela, P. Neittaanmaki and J. Periaux), John Wiley & Sons, Ltd., Jyvaskyla, Finland, May 30 - June 3, 1999, pp. 231-260. [32]
- [20] Martin, T.J., Dulikravich, G.S., Han, Z.-X. & Dennis, B.H., Minimizing Coolant Mass Flow Rate in Internally Cooled Gas Turbine Blades, ASME paper 99-GT-146, *ASME Turbo Expo '99*, Indianapolis, Indiana, June 7-10, 1999. [33]
- [21] [34]
- [22] [35]
- [23] [36]
- [24] [37]
- [25] [38]
- [26]
- [27]
- [28]
- [29]
- [30]
- [31]
- [32]
- [33]
- [34]
- [35]
- [36]
- [37]
- [38]



- [21] Press, W.H., Teukolsky, S.A., Vetterling, W.T. & Flannery, B.P., *Numerical Recipes in FORTRAN, The Art of Scientific Computing*, 2nd Edition, Cambridge University Press, Cambridge, 1986.
- [22] Petrovic, M.V., Dulikravich, G.S. & Martin, T.J., Maximizing Multistage Turbine Efficiency by Optimizing Hub and Shroud Shapes and Inlet and Exit Conditions of Each Blade Row, ASME paper 99-GT-071, *ASME Turbo Expo '99*, Indianapolis, Indiana, June 7-10, 1999.
- [23] Dennis, B.H., Dulikravich, G.S. & Han, Z.-X., Constrained Optimization of Turbomachinery Airfoil Cascade Shapes Using a Navier-Stokes Solver and a Genetic/SQP Algorithm, ASME paper 99-GT-441, *ASME Turbo Expo '99*, Indianapolis, Indiana, U.S.A., June 7-10, 1999.
- [24] Foster, N.F. & Dulikravich, G.S., Three-Dimensional Aerodynamic Shape Optimization Using Genetic and Gradient Search Algorithms, *AIAA Journal of Spacecraft and Rockets*, Vol. 34, No. 1, pp. 36-42, January-February 1997.
- [25] Dowell, E.H., Nonlinear Aeroelasticity, *Flight-Vehicle Materials, Structures, and Dynamics, Vol. 5, Part II, Structural Dynamics and Aeroelasticity*, (eds A.K. Noor and S.L. Venneri), ASME, New York, NY, 1993.
- [26] Barsky, B.A., *Computer Graphics and Geometric Modeling Using Beta-Splines*, Springer-Verlag, Berlin, Germany, 1988.
- [27] Davidon, W.C., Variable Metric Method for Minimization, Atomic Energy Commission Research and Development Report, *ANL-5990 (Rev.)*, November 1959.
- [28] Goldberg, D.E. *Genetic Algorithms in Search, Optimization and Machine Learning*, Addison-Wesley, 1989.
- [29] Nelder, J.A. & Mead, R., A Simplex Method for Function Minimization, *Computer Journal*, Vol. 7, pp. 308-313, 1965.
- [30] Haftka, R.T. and Gurdal, Z., *Elements of Structural Optimization*, 3rd edition, Kluwer Academic Publishers, Boston, MA, 1992.
- [31] Kerrebrock, J.L., *Aircraft Engines and Gas Turbines*, MIT Press, Cambridge, MA, 1977.
- [32] Li, H. & Kassab, A.J., A Coupled FVM/BEM Approach to Conjugate Heat Transfer in Turbine Blades, AIAA Paper 94-1981, *6th AIAA/ASME Joint Thermophysics and Heat Transfer Conference*, Colorado Springs, CO, June 20-23, 1994.
- [33] Li, H. & Kassab, A.J., Numerical Prediction of Fluid Flow and Heat Transfer in Turbine Blades with Internal Cooling, AIAA paper 94-2933, *30<sup>th</sup> AIAA/ASME/SAE/ASEE Joint Propulsion Conference*, Indianapolis, IN, June 27-29, 1994.
- [34] Han, Z.-X. & Liu, Z.-J., Numerical Calculation of 2-D Inviscid Flow-Fields on Unstructured Grids, *Journal of Engineering Thermophysics*, Vol. 18, No.6, November 1997.
- [35] Chima, R.V., Explicit Multigrid Algorithm for Quasi-Three-Dimensional Viscous Flows in Turbomachinery, *Journal of Propulsion and Power*, Vol. 3, No. 5, pp. 397, September-October 1987.
- [36] Brebbia, C.A., *The Boundary Element Method for Engineers*, John Wiley & Sons, New York, NY, 1978.
- [37] Telles, J.C.F. A Self-adaptive Coordinate Transformation for Efficient Numerical Evaluation of General Boundary Element Integrals, *International Journal of Numerical Methods in Engineering*, Vol. 24, pp. 959-973, 1987.
- [38] Aliabadi, M.H. & Mellings, S.C., Boundary Element Formulations for Sensitivity Analysis and Crack Identification, in *Boundary Integral Formulations for Inverse*

- Analysis*, (eds D.B. Ingham and L.C. Wrobel), Computational Mechanics Publications, Southampton, 1997.
- [39] White, F.M., *Heat and Mass Transfer*, Addison-Wesley, Reading, MA, 1988.
  - [40] Holman, J.P., *Heat Transfer, Fifth Edition*, McGraw Hill Book Company, 1981.
  - [41] Webb, R.L., *Principles of Enhanced Heat Transfer*, John Wiley & Sons, Inc., New York, NY, 1998.
  - [42] Schlichting, H., *Boundary Layer Theory* (translated by Kestin, J.), McGraw Hill Book Co., New York, NY, 1979.
  - [43] Dipprey, D.F. & Sabersky, R.H., Heat and Momentum Transfer in Smooth and Rough Tubes at Various Prandtl Number, *International Journal of Heat and Mass Transfer*, Vol. 6, pp. 329-353, 1963.
  - [44] Saad, M.A., *Compressible Fluid Flow, Second Edition*, Prentice Hall, Englewood Cliffs, NJ, 1993.
  - [45] Rizzo, F.J. & Shippy, D.J., An Advanced Boundary Integral Equation Method for Three-dimensional Thermo-elasticity, *International Journal of Numerical Methods in Engineering*, Vol. 11, pp. 1753-1768, 1977.
  - [46] Brebbia, C.A. & Dominguez, J., *Boundary Elements, An Introductory Course*, McGraw-Hill Book Company, New York, NY, 1989.
  - [47] Cruse, T.A., Boundary Integral Equation Method for Three-Dimensional Elastic Fracture Mechanics Analysis, Pratt and Whitney Aircraft Report AFOSR-TR-75-0813, 1975.
  - [48] Meric, R.A. Differential and Integral Sensitivity Formulations and Shape Optimization by BEM, *Engineering Analysis with Boundary Elements*, Vol. 15, pp. 181-188, 1995.
  - [49] Hafka, R.T. & Malkus, D.S., Calculation of Sensitivity Derivatives in Thermal Problems by Finite Differences, *International Journal of Numerical Methods in Engineering*, Vol. 17, pp. 1811-1821, 1981.
  - [50] Kane, J.H. & Saigal, S., Design Sensitivity Analysis of Solids Using BEM, *Journal of Engineering Mechanics*, ASCE, Vol. 114, No. 10, pp. 1703-1722, 1988.
  - [51] Yamazaki, K., Sakamoto, J. & Kitano, M., Three-Dimensional Shape Optimization Using the Boundary Element Method, *AIAA Journal*, Vol. 32, No. 6, June, 1994.
  - [52] Guiggiani, M., Krishnasamy, G., Rudolphi, T.J. & Rizzo, F.J., A General Algorithm for the Numerical Solution of Hyper-singular Boundary Element Integral Equations, *ASME Journal of Applied Mechanics*, Vol. 59, pp. 604-614, 1992.
  - [53] Arts, T., Lambert de Rouvroit, M. & Rutherford, A.W., Aero-Thermal Investigation of a Highly Loaded Transonic Linear Turbine Guide Vane Cascade, von Karman Institute for Fluid Dynamics, *Technical Note 174*, September 1990.

Cha

Dua  
andM.H.  
Depar  
Unive

Abst

This cl  
and th  
analysi  
incorpe  
ture ar  
applic  
aries, t  
to dem  
and tra

1 I

In sens  
to sud  
failure  
for the  
The  
for the  
of this  
leads to  
The di  
dimens  
problem  
equatic  
on one  
The